



HAL
open science

Numerical modeling and analysis of the ballistic impact response of ceramic/composite targets and the influence of cohesive material parameters

Ibrahim Goda, Jérémie Girardot

► **To cite this version:**

Ibrahim Goda, Jérémie Girardot. Numerical modeling and analysis of the ballistic impact response of ceramic/composite targets and the influence of cohesive material parameters. *International Journal of Damage Mechanics*, 2021, 7 (30), pp.1079-1122. 10.1177/1056789521992107 . hal-03312436

HAL Id: hal-03312436

<https://hal.inrae.fr/hal-03312436>

Submitted on 19 Jan 2022

HAL is a multi-disciplinary open access archive for the deposit and dissemination of scientific research documents, whether they are published or not. The documents may come from teaching and research institutions in France or abroad, or from public or private research centers.

L'archive ouverte pluridisciplinaire **HAL**, est destinée au dépôt et à la diffusion de documents scientifiques de niveau recherche, publiés ou non, émanant des établissements d'enseignement et de recherche français ou étrangers, des laboratoires publics ou privés.

Numerical modeling and analysis of the ballistic impact response of ceramic/composite targets and the influence of cohesive material parameters

Ibrahim Goda  and Jérémie Girardot

Abstract

Hybrid ceramic/composite targets are acknowledged to provide effective impact protection against armor piercing projectiles, which is why the research on this topic is continuously developing further. In this work, a nonlinear dynamic finite element (FE) simulation method is developed to systematically explore the ballistic perforation behaviors of hybrid ceramic/woven-fabric reinforced polymer (WFRP) composite when impacted by a non-deformable projectile. The hybrid system is composed by an alumina ceramic plate forming the front surface and glass or carbon WFRP composite back-up plate. The simulations are carried out using ABAQUS/Explicit FE code, wherein three different constitutive material models are formulated and implemented. The Johnson–Holmquist and composite damage models are used for alumina and composite material behaviors, respectively. The brittle fracture and fragmentation of the ceramic plate and the failure criteria based on fracture of fibers or matrices of composite materials during perforation are considered. Besides, interlaminar delamination between composite plies as well as ceramic/composite interfacial decohesion are modeled using a cohesive surface method, and the behaviors of interlayer degradation and failure are described using a traction-separation law. The accuracy of the developed model is validated with available experimental and analytical results. What's more, the perforation process against the projectile and the ballistic mechanism of each layer in the composite backplate and in the ceramic as well are profoundly explored. Meanwhile, the numerical simulations are used to evaluate the changes of energy of the projectile and ceramic/composite panels. The influence of key parameters, such as interface cohesive properties and friction, on the ballistic performance in terms of energy absorption capability is additionally addressed. For the preliminary and early design phase, the present dynamic model could provide an efficient approach for numerical predictions of ballistic impact responses of the hybrid ceramic/FRP composites.

Arts et Metiers Institute of Technology, University of Bordeaux, Bordeaux, France

Corresponding author:

Ibrahim Goda, Arts et Metiers Institute of Technology, University of Bordeaux, CNRS, Bordeaux INP, INRAE, HESAM Université, I2M Bordeaux, F-33400 Talence, France.
Email: ibrahim.goda02@gmail.com

Keywords

Ballistic impact, damage constitutive models, finite element analysis, ceramic/composite panels, polymeric composites, energy dissipation

Introduction

Fiber reinforced polymer (FRP) composite materials are widely employed in a variety of commercial and military applications such as automotive, protective armors, aerospace and marine engineering (Bai and Jin, 2016; Bondrya et al., 2015; Goda et al., 2019). The necessity of these materials has been increased due to their advantages of high stiffness-to-weight and high strength-to-weight ratios, corrosion resistance, impact resistance and energy absorption capacities (Park and Seo, 2012; Wang et al., 2016). Particularly, in areas that are prone to impact damage, the use of composite materials requires special attention. More specifically, the knowledge of impact dynamic behavior of the composite materials and their damage resistance is substantial in order to optimize the structure regarding its impact resistance. Based on the energy transfer between the projectile and target, energy dissipation and damage propagation mechanisms, the impact load with respect to velocity can be broadly categorized into four classifications: low-velocity, high-velocity, ballistic-velocity, and hyper-velocity impacts (Safri et al., 2018). Overall, according to the literature, the impact events may be simplified by grouping them into two distinct cases, namely, low-velocity impact by a large mass and high-velocity impact by a small mass. The second case is the one of interest in this work.

One of the weak points of FRP composite panels is their vulnerability against armor piercing projectiles (Liu et al., 2015). To overcome such problem, hard faced panels with a laminated composite backing are commonly used. Indeed, with the requirements of more efficient lightweight armor systems, the nonmetallic materials of ceramics are commonly used in combination with laminate composites for ballistic protection of civilian and military equipment, where the mobility is essential (Rahbek and Johnsen, 2019; Zaera, 2011). Hybrid armors made of a ceramic front plate and a back laminated composite plate, seem to form a very efficient shield against ballistic impact, since they combine low density, high hardness, high rigidity and high inherent compressive strength of ceramic with the lightweight and ductility of composite laminates. Alumina (Al_2O_3), Boron Carbide (B_4C), Silicon Carbide (SiC) and Aluminum nitride (AlN) are the most widely employed ceramic materials in the ballistic armor systems (Garcia-Avila et al., 2015; Jena et al., 2010). With respect to the back laminate layers, composite laminates based on kevlar, glass, polyethylene, and carbon fiber materials arranged in unidirectional or woven textiles within a polymer thermoset or thermoplastic, are the most widely used in these applications (Bandaru and Ahmad, 2013; Bandaru et al., 2015; Kulkarni et al., 2013; Naik and Shrirao, 2004; Pandya et al., 2013; Silva et al., 2005; Tham et al., 2008; Walsh et al., 2005; Yen, 2012).

When a projectile impacts onto ceramic/composite, the front ceramic plate first helps erode and blunt the projectile tip and the reflected tensile wave breaks the ceramic in a brittle manner. Then, the backing composite plate deforms to absorb the remaining kinetic energy of the decelerated projectile, and simultaneously holds the ceramic and projectile fragments to prevent them from causing further damage (Krishnan et al., 2010; Signetti and Pugno, 2014). Broadly, ceramic materials play a major role in impact resistance due to their high strength and hardness properties as reported in Krell and Strassburger (2008). The possible damages that may occur in ceramic tiles under ballistic impact are mainly in the forms of tensile failure, transverse cracking, shear plugging

and pulverization (Shanazari et al., 2017). When reaching the composite layer, it passes also into a very complex ballistic penetration mechanisms. Generally, the ballistic impact response of laminated composites is a challenging problem, and it has attracted the attention of a number of researchers. For example, in Naik and Shrirao (2004), Bandaru and Ahmad (2013), Yen (2012), Silva et al. (2005), Tham et al. (2008), Kulkarni et al. (2013), Walsh et al., 2005, and Naik and Doshi (2004), the ballistic impact response of both thermoset and thermoplastic composite laminates, are investigated through experiments, numerical simulations, and analytical models. After a thorough literature review, it is found that the most of published studies on impact of FRP composite materials are in fact based on low velocity impact events with relatively high masses and low impact velocities (Heimba et al., 2009; Hongkarnjanakul et al., 2013; Kursun and Senel, 2013; Li et al., 2019; Liao and Jia, 2018; Lopes et al., 2009; Mikkor et al., 2006; Mitrevski et al., 2006; Schoeppner and Abrate, 2000; Tan et al., 2015; Tita et al., 2008). On the other hand, there are not so many researches as compared to that of low-velocity impact, on the high-velocity impact behavior of FRP composites (Higuchi et al., 2017; López-Puente et al., 2007; Pernas-Sánchez et al., 2014; Schwab et al., 2018; Yamada et al., 2011). Besides, the main characteristic that influences the impact in composite materials is the fracture toughness of the resin system; the improvement in the matrix fracture toughness results in raising the resistance of the composite to the onset of interlaminar delamination induced by matrix cracking (Andrew et al., 2019).

Designing of such hybrid ceramic/composite targets based solely on the experimental data requires massive materials and manpower, which can be time consuming and uneconomical. Therefore, the need for developing accurate predictive simulation tools becomes more crucial. More particularly, since the ballistic ceramic/composite materials pass into a very complex ballistic penetration mechanisms when impacted with high velocity projectiles, they indeed need a complete and quantitative analysis for a better understanding. For such a need, the adoption of numerical modeling approaches would allow to derive and understand the constitute relation, and understand of the influence of each considered parameter and simulate the overall ballistic materials behavior in response to ballistic impact, leading ultimately to an effective design for enhanced ballistic resistant target. Although there are numerous studies on the ballistic impact behavior of composite, ceramic, and ceramic/metal targets (e.g. Sastry et al., 2014; Serjouei et al., 2015; Yossifon et al., 2002; Zhang and Li, 2010; Zinszner et al., 2015), only a few studies reported on the ballistic impact performance of the ceramic/composite targets (Benloulo and Sanchez-Galvez, 1998; Fawaz et al., 2004; Feli et al., 2011; Naik et al., 2013; Shokrieh and Javadpour, 2008; Talib et al., 2012; Tasmemirci et al., 2012). Benloulo and Sanchez-Galvez (1998) developed an analytical model to simulate the ballistic performance of ceramic/composite armors, wherein the back plate of the armor is made of polymer composite material. Also, Naik et al. (2013) presented an analytical model for the ballistic impact behavior of ceramic/composite targets; this model is based on wave theory and energy balance between the kinetic energy of the projectile and the energy absorbed by the target. Feli et al. (2011) also formulated an analytical model for the perforation of ceramic/multi-layer woven fabric targets by blunt projectiles. Talib et al. (2012) studied the effect of high velocity ballistic impact on woven fiber Kevlar-29 and Al₂O₃ powder/epoxy composites both theoretically and experimentally. Shokrieh and Javadpour (2008) modeled the B4C/Kevlar 49 fiber epoxy composite armor to investigate the penetration of a projectile under oblique and normal impact conditions. Tasmemirci et al. (2012) investigated experimentally and numerically the effects of various interlayer materials on the ballistic performance of Ceramic/S2-Glass-SC 15 epoxy composite armor. Fawaz et al. (2004) developed three-dimensional finite element models to investigate the performance of ceramic/composite armors when subjected to normal and oblique penetrating projectiles. Even though there are typical studies on ballistic impact behavior of ceramic/composite targets, it can

be seen that in most of the published studies, the damage and energy absorbing mechanisms of the composite backplates undergoing ballistic impact and penetration have not yet been clearly addressed.

The main objective and contribution of the present work is thus to provide a fully three-dimensional nonlinear dynamical FE model for ballistic impact simulations of hybrid ceramic/woven-fabric laminate composite targets with a non-intrusive approach, i.e. using user defined material models within the FEM package ABAQUS/Explicit. In this way, a theoretical framework and numerical scheme, based on the combination of strain rate and pressure dependent Johnson–Holmquist plasticity damage model for the ceramic layer, damage initiation criteria and damage evolution law based on elastic damage and plastic deformation theories for laminated composite, and surface-based cohesive zone model using traction-separation based constitutive law for the interfacial debonding between adjacent layers, all together are set up to comprehensively investigate the ballistic penetration behaviors and evaluate the energy absorption capability of the a two-plated structure of ceramic and composite materials. The proposed developments are first validated with available experimental and analytical results before they are used in numerical simulations and parametric analyses.

Through numerical analysis for the proposed ceramic material type and proposed composite lamination schemes, significant insights into perforation resistance mechanism, energy dissipation mechanism and stress distribution are gained. This study focuses on these trends in order to evaluate the influence of failure mechanism of ceramic/composite panels on the energy absorption of the projectile, thereby the dissipated energy can be maximized. Concomitantly, we perform numerical simulations to evaluate the impact force and residual velocity of projectile versus time at different ballistic impact energies. For further understand the damage behaviors within the composite laminate, the projected areas of intraply damage due to fiber tension, fiber compression and matrix shear as well as the projected interlaminar delamination area are thoroughly examined. We finally further investigate influence of key parameters such as interfacial cohesive properties and friction coefficients on the ballistic performance of the hybrid ceramic/composite materials.

Constitutive relations and failure models

In this study, the Johnson–Holmquist brittle material model is used for modeling ceramic plate on the front side of the target. Whereas, composite damage material model is used for modeling composite laminates on the backside of the target. In addition, cohesive zone model is employed to describe the interlaminar damage between layers within the laminate and debonding behavior between the ceramic and composite. The constitutive equations of these models are exposed in the sequel.

Johnson–Holmquist model of the ceramic

The Johnson-Holmquist material model (JH-2) is a constitutive model suitable for predicting the behavior of brittle materials subjected to extreme loading conditions (Johnson and Holmquist, 1994). The JH-2 model is commonly used to describe the behavior of ceramics under ballistic impact that are subjected to loading conditions that involve high strain rates, high pressures and large deformations. The JH-2 model consists of three principle components: a representation of the intact and fractured strength in the form of a pressure-dependent yield surface, a damage model that transitions the ceramic material from the intact state to a fractured state, and an equation of state (EOS) for the pressure-volume relationship that can include dilation (or bulking) effects.

Regarding the first part of the model, the strength of the ceramic material is expressed in terms of the normalized von Mises equivalent stress, σ , as

$$\sigma^* = \sigma_i^* - D(\sigma_i^* - \sigma_f^*) \quad (1)$$

where σ_i^* is the normalized intact equivalent stress, σ_f^* is the normalized fractured equivalent stress, and D is the damage variable varying between 0 and 1. For the intact (undamaged) state, $D = 0$, whereas for a fully damaged state $D = 1$. Note that the normalized equivalent stresses in the previous equation (σ^* , σ_i^* and σ_f^*) have the general form $\sigma^* = \sigma/\sigma_{HEL}$, where σ is the actual von Mises equivalent stress and σ_{HEL} is the equivalent stress at the Hugoniot elastic limit (HEL). The actual equivalent stress is calculated by the formula of von Mises stress as follows

$$\sigma = \sqrt{\frac{1}{2} \left[(\sigma_x - \sigma_y)^2 + (\sigma_x - \sigma_z)^2 + (\sigma_y - \sigma_z)^2 + 6(\tau_{xy}^2 + \tau_{xz}^2 + \tau_{yz}^2) \right]} \quad (2)$$

where σ_x , σ_y , and σ_z are the normal stresses, τ_{xy} , τ_{xz} , and τ_{yz} are the shear stresses.

The normalized intact and fractured equivalent stresses can be respectively expressed as functions of the pressure and strain rate as following

$$\sigma_i^* = A(P^* + T^*)^N (1 + C \ln \dot{\epsilon}^*) \quad \text{represents the undamaged behavior} \quad (3)$$

$$\sigma_f^* = B(P^*)^M (1 + C \ln \dot{\epsilon}^*) \leq \sigma_f^{\max} \quad \text{represents the damage behavior} \quad (4)$$

where A , B , C , M , N and σ_{HEL} are all material parameters. $P^* = P/P_{HEL}$ refers to the normalized pressure where P is the actual pressure and P_{HEL} is the pressure at the HEL. $T^* = T/P_{HEL}$ stands for the normalized maximum tensile hydrostatic pressure, in which T is the maximum hydrostatic tensile pressure that the ceramic material can withstand. $\dot{\epsilon}^* = \dot{\epsilon}/\dot{\epsilon}_0$ and σ_f^{\max} refer respectively to the normalized strain rate and maximum normalized fracture strength (ultimate value of σ_f^*), with $\dot{\epsilon}$ the actual equivalent strain rate and $\dot{\epsilon}_0$ is the reference strain rate (typically set to 1.0 s^{-1}).

In Figure 1, we provide a schematic diagram of the JH-2 strength model that describes the material strength curve on three sides: the intact, damaged, and fractured state. As depicted in Figure 1, each state has its own strength equation which illustrates the relation of normalized equivalent stress versus normalized pressure.

Regarding the evolution/accumulation of damage D , it is formed as the incrementally increasing function

$$D = \sum \frac{\Delta \epsilon^p}{\epsilon_f^p} \quad \text{represents the accumulated damage} \quad (5)$$

The term $\Delta \epsilon^p$ refers to the increment in equivalent plastic strain during a cycle of integration and ϵ_f^p stands for the equivalent plastic strain required to cause fracture of the ceramic material at a constant pressure. The expression for ϵ_f^p is given as follows

$$\epsilon_f^p = D_1 (P^* + T^*)^{D_2} \quad (6)$$

where D_1 and D_2 are the damage constants for ϵ_f^p .

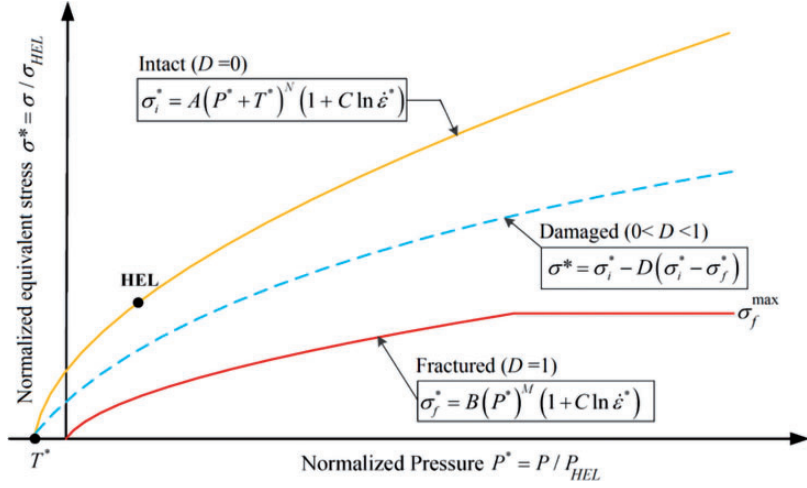


Figure 1. A schematic representation of the JH-2 strength model.

The model considers that the damage variable increases gradually with plastic deformation; $D = 1$, the material fails immediately, and $D = 0$ the material preserves its intact strength.

Within the JH-2 model, the polynomial EOS presents the relationship between hydrostatic pressure, P and volumetric strain, μ . The hydrostatic pressure in undamaged material ($D = 0$) is given by the following equation

$$P = K_1\mu + K_2\mu^2 + K_3\mu^3, \quad \mu > 0 \quad (\text{hydrostatic compression}) \quad (7)$$

and for tensile pressure, it is followed by this equation

$$P = K_1\mu, \quad \mu < 0 \quad (\text{hydrostatic tension}) \quad (8)$$

where μ is defined as $\mu = \rho/\rho_0 - 1 = V_0/V - 1$, therein ρ and V are the current density and volume, and ρ_0 and V_0 are the reference or initial density and volume, respectively. K_1 is the initial bulk modulus, K_2 and K_3 are the equation-of-state coefficients.

After damage begins to accumulate ($D > 0$), bulking can occur and equation (7) shall be modified to include the effect of bulking. The modified polynomial EOS includes the effects of dilation or bulking that occur when brittle materials fail by including an additional incremental pressure, ΔP , is then given by

$$P = K_1\mu + K_2\mu^2 + K_3\mu^3 + \Delta P \quad (0 < D \leq 1), \quad \mu > 0 \quad (9)$$

The bulking induced pressure increment, ΔP , is determined from energy considerations and it varies from $\Delta P = 0$ at $D = 0$ to $\Delta P = \Delta P_{\max}$ at $D = 1$. The decrease in strength when the material goes from an intact state to a failed state produces a decrease in the deviatoric elastic energy, ΔU . This loss of elastic energy is converted to an increase in potential hydrostatic energy by incrementally increasing ΔP according to

$$\Delta P_{t+\Delta t} = -K_1\mu_{t+\Delta t} + \sqrt{(K_1\mu_{t+\Delta t} + \Delta P_t)^2 + 2\beta K_1\Delta U} \quad (10)$$

The parameter β is the fraction of the deviatoric elastic energy loss converted to potential hydrostatic energy ($0 \leq \beta \leq 1$). For further details about the model formulation, the reader is referred to Johnson and Holmquist (1994).

Fabric reinforced composites constitutive model

This subsection is dedicated to describe the constitutive model used for simulating the fabric reinforced back laminate layers. Each ply in the composite laminate is modeled as a homogeneous orthotropic elastic or elastic-plastic material with the capability to sustain progressive stiffness degradation due to fiber/matrix cracking, and plastic deformation under shear loading. Thereupon, the present model includes an elastic damage model in the fiber directions along with an elastic-plastic damaging model for inelastic shear effects. These different aspects will be explicated in the sequel.

Elastic continuum damage mechanics. In a local coordinate system with the base vectors aligned with the fiber directions, the constitutive stress-strain relations under plane stress conditions are formulated. The elastic strain-stress relations for an orthotropic material coupled to damage then takes the following form, expressed in terms of internal damage parameters (d_i) as (Johnson, 2001)

$$\underbrace{\begin{Bmatrix} \varepsilon_{11} \\ \varepsilon_{22} \\ \varepsilon_{12}^e \end{Bmatrix}}_{\varepsilon} \begin{bmatrix} \frac{1}{(1-d_1)E_1} & \frac{-\nu_{12}}{E_1} & 0 \\ \frac{-\nu_{21}}{E_2} & \frac{1}{(1-d_2)E_2} & 0 \\ 0 & 0 & \frac{1}{(1-d_{12})2G_{12}} \end{bmatrix} \underbrace{\begin{Bmatrix} \sigma_{11} \\ \sigma_{22} \\ \sigma_{12} \end{Bmatrix}}_{\sigma} \quad (11)$$

where ε and σ are the elastic strain and stress tensors; they are written in vector format as $\{\varepsilon_{11} \ \varepsilon_{22} \ \varepsilon_{12}^e\}^T$ and $\{\sigma_{11} \ \sigma_{22} \ \sigma_{12}\}^T$, respectively. Since the plastic deformation is considered in shear, therefore, the superscript “e” is used to represent the elastic deformation. E_1 and E_2 are the Young’s moduli in the principal orthotropic directions, ν_{12} and ν_{21} are the principal Poisson’s ratios, and G_{12} is the in-plane shear modulus. d_1 and d_2 are damage variables associated with the fiber fracture along the principal orthotropic directions 1 and 2, respectively, and d_{12} is the damage variable associated with the matrix damage (or micro-cracking) due to the shear deformation. The damage parameters vary between 0 (undamaged state) and 1 (fully damage state) and represent stiffness matrix degradation caused by different loading conditions due to micro-damage in the material.

Note that the failure in the principal directions 1 and 2 are fiber dominated and can occur either in tension or compression, while in shear, damage is considered matrix dominated, as will be described subsequently.

Fiber damage model. In this model, the tensile and compressive fiber failure modes are distinguished. The model tracks damage caused by tension loads separately from damage caused by compression loads. Accordingly, the corresponding damage variables (d_i) associated with longitudinal and transverse damage are defined based on the stress state in the fiber directions 1 and 2 as follows

$$d_1 = d_{1+} \frac{\langle \sigma_{11} \rangle}{|\sigma_{11}|} + d_{1-} \frac{\langle -\sigma_{11} \rangle}{|\sigma_{11}|}; d_2 = d_{2+} \frac{\langle \sigma_{22} \rangle}{|\sigma_{22}|} + d_{2-} \frac{\langle -\sigma_{22} \rangle}{|\sigma_{22}|} \quad (12)$$

where d_{i+} and d_{i-} are the tensile and compressive damage variables of the fibers in the i th directions ($i=1,2$), respectively. $\langle x \rangle$ refers to the McCauley operator, defined as $\langle x \rangle = (x + |x|)/2$. Here and thereafter, the subscript “1+, 1-, 2+, 2-” is used to denote tensile (+) or compressive (-) failure in the 1 and 2 directions.

The material behavior along fiber directions is characterized by damaged elasticity. Thereby, the fiber damage variables are considered to evolve as a function of the corresponding effective (undamaged) normal stress in the following forms

$$d_{1+} = d_{1+}(\tilde{\sigma}_{1+}), \quad d_{1-} = d_{1-}(\tilde{\sigma}_{1-}), \quad d_{2+} = d_{2+}(\tilde{\sigma}_{2+}), \quad d_{2-} = d_{2-}(\tilde{\sigma}_{2-}) \quad (13)$$

where $\tilde{\sigma}_{i+}$ and $\tilde{\sigma}_{i-}$ ($i=1,2$) are the effective tensile and compressive stresses, defined as

$$\tilde{\sigma}_{1+} = \frac{\langle \sigma_{11} \rangle}{(1 - d_{1+})}, \quad \tilde{\sigma}_{1-} = \frac{\langle -\sigma_{11} \rangle}{(1 - d_{1-})}, \quad \tilde{\sigma}_{2+} = \frac{\langle \sigma_{22} \rangle}{(1 - d_{2+})}, \quad \tilde{\sigma}_{2-} = \frac{\langle -\sigma_{22} \rangle}{(1 - d_{2-})} \quad (14)$$

At any given time, the elastic domain where the material may be elastic damaging, is defined in terms of the damage activation functions, F_i , associated with damage in the fiber direction-1 ($i=1\pm$) and fiber direction-2 ($i=2\pm$) as follows

$$F_{i+} = \phi_{i+} - \lambda_{i+} \leq 0, \quad F_{i-} = \phi_{i-} - \lambda_{i-} \leq 0 \quad (15)$$

In equation (15), the damage state is characterized by the loading functions ϕ_{i+}, ϕ_{i-} ($i=1, 2$) for different failure mechanisms. These functions provide four criteria for describing the initiation of fiber failure in directions 1 and 2, and are given by

$$\phi_{i+} = \frac{\tilde{\sigma}_{i+}}{X_{i+}}, \quad \phi_{i-} = \frac{\tilde{\sigma}_{i-}}{X_{i-}} \quad (16)$$

where ϕ_{i+} and ϕ_{i-} ($i=1, 2$) represent the tensile and compressive damage modes along fiber directions 1 and 2, respectively. X_{i+} and X_{i-} ($i=1, 2$) refer to the tensile and compressive strengths, respectively, for uniaxial loading along the fiber directions 1 and 2.

λ_{i+} and λ_{i-} in equation (15) are the tensile and compressive damage thresholds, respectively. Material damage is activated when the value of ϕ_i reaches the damage threshold λ_i ($i=1\pm, 2\pm$). The damage thresholds λ_i take an initial value of unity when the material is undamaged. After damage initiation, i.e., when $\phi_{i+} = 1$ or/and $\phi_{i-} = 1$ ($i=1, 2$), they increase with damage evolution according to

$$\lambda_{i+}(t) = \max_{\tau \leq t} \phi_{i+}(\tau), \quad \lambda_{i-}(t) = \max_{\tau \leq t} \phi_{i-}(\tau) \quad (17)$$

This definition ensures that the damage thresholds for each loading condition are non-decreasing quantities, such that $\dot{\lambda}_i(t) \geq 0$ ($i=1\pm, 2\pm$). Besides, the evolution of the damage threshold values is assumed to fulfill the Kuhn-Tucker complementary conditions ($F_i \leq 0, \dot{\lambda}_i F_i = 0$) and the consistency condition ($\dot{\lambda}_i \dot{F}_i = 0$) (Maimí et al., 2006).

Once the damage initiation criterion is met, then further damage progression can be developed. The way by which the damage will progress depends on the level of the stress caused by the strain

increment. Since damage is irreversible, the damage evolution rate shall satisfy the following condition: $\dot{d}_i \geq 0$. The exponential damage evolution law is adopted for each damage variable d_i ($i = 1\pm, 2\pm$) and expressed in the following form (Maimí et al., 2006)

$$d_i = 1 - \frac{1}{\lambda_i} \exp \left[\frac{-2g_0^i L_c}{G_f^i - g_0^i L_c} (\lambda_i - 1) \right] \quad (18)$$

where g_0^i is the elastic strain energy density (elastic energy per unit volume) at the point of damage initiation expressed as $g_0^i = X_i^2/2E_i$, L_c is the characteristic element size, and G_f^i is the fracture energy per unit area under uniaxial tensile or compressive loading.

It shall be noticed that the above formulation of the damage evolution model ensures that the damage parameters are monotonically increasing quantities, such that $\dot{d}_i \geq 0$. Also the model ensures that when the lamina is subjected to uniaxial loading conditions along the fiber directions 1 and 2, the right amount of energy will be dissipated during the material fracture regardless of the element size (Johnson and Simon, 1999). This is achieved through incorporating the characteristic element length L_c in the damage evolution formulation, where imposing a restriction on the maximum element size $L_c < L_{\max} = G_f^i/g_0^i$ leads to accurate capture of the correct amount of energy dissipation during fracture.

Combined elastoplastic shear damage model. The fabric ply constitutive model presented in the previous subsections is adopted for an elastic damaging material, which is appropriate for fiber dominated failure modes that involve tensile and compressive loadings along fiber directions. Herein, a coupled elastoplastic damage constitutive model suitable for predicting the damage initiation and post-failure behavior of fabric composite materials that exhibit irreversible strains caused by plasticity effects under shear loading is established.

Within that scope, the matrix damage response under shear loading will include stiffness degradation due to matrix microcracking as well as plastic deformation (Phadnis et al., 2013). Therefore, the shear strain is presented as a sum of the elastic and plastic shear strain parts ε^e and ε^p as follows

$$\varepsilon_{12} = \varepsilon_{12}^e + \varepsilon_{12}^p \quad (19)$$

From equations (11) and (19), the effective shear stress is expressed in terms of elastic or plastic shear strain as follows

$$\tilde{\sigma}_{12} = \frac{\sigma_{12}}{(1 - d_{12})} = 2G_{12}\varepsilon_{12}^e = 2G_{12}(\varepsilon_{12} - \varepsilon_{12}^p) \quad (20)$$

The plastic deformation is considered to occur in the undamaged area of the damaged composite. According to this, the yield criterion, the hardening law and plastic flow rule are expressed in terms of effective shear stress $\tilde{\sigma}_{12}$ and equivalent plastic strain due to shear deformation $\bar{\varepsilon}^p$.

In effective stress space, the plastic yield function, F , is expressed as follows

$$|\tilde{\sigma}_{12}| - \tilde{\sigma}_0(\bar{\varepsilon}^p) \leq 0 \quad (21)$$

The hardening function $\tilde{\sigma}_0(\bar{\varepsilon}^p)$ is taken to be in the following form

$$\tilde{\sigma}_0(\bar{\varepsilon}^p) = \tilde{\sigma}_{y,0} + C(\bar{\varepsilon}^p)^\gamma \quad (22)$$

where $\tilde{\sigma}_{y0}$ is the initial effective shear yield stress, C and γ are material constants. The associated plastic flow rule, the plastic strain rate $\dot{\bar{\epsilon}}^p$, is expressed as

$$\dot{\bar{\epsilon}}_{12}^p = \dot{\bar{\epsilon}}^p \frac{\partial F}{\partial \tilde{\sigma}_{12}} = \dot{\bar{\epsilon}}^p \text{sign}(\tilde{\sigma}_{12}) \quad (23)$$

In the same manner as for tensile and compressive fiber damage, the damage activation function under shear load takes the following form

$$F_{12} = \phi_{12} - \lambda_{12} \leq 0 \quad (24)$$

where the function ϕ_{12} is introduced to provide a criterion for initiation of shear damage of the matrix, which is expressed as follows

$$\phi_{12} = \frac{\tilde{\sigma}_{12}}{S_{12}} \quad (25)$$

with S_{12} the material shear strength or rather the shear stress required for initiation of matrix damage.

Shear damage development is initiated when the function ϕ_{12} reaches the damage threshold, i.e., $\phi_{12} = \lambda_{12}$. The initial damage threshold λ_{12} for matrix damage is set to one and increases with increasing matrix damage in accordance with

$$\lambda_{12}(t) = \max_{\tau \leq t} \phi_{12}(\tau) \quad (26)$$

Lastly, based on the works in Maimí et al. (2006) and Johnson and Simon (1999), it is considered that the shear damage variable d_{12} increases with the logarithm of λ_{12} until a maximum value of d_{12} is attained. Therefore, the evolution of the shear damage variable is given by

$$d_{12} = \min\left(\alpha_{12} \ln(\lambda_{12}), d_{12}^{\max}\right) \quad (27)$$

with $\alpha_{12} > 0$ shear damage parameter and $d_{12}^{\max} \leq 1$ the maximum shear damage.

Cohesive zone damage model

In the present study, we use the cohesive zone method (CZM) to model the delamination between the layers of woven fabric laminates as well as the debonding between the ceramic plate and the composite backing plate. The principle of this method is the cohesive behavior interaction of two adjacent surfaces, where the contact between adhesive surfaces is defined as a surface interaction property with a zero interface thickness. This method follows a traction-separation damage law, in which the traction stress and separation displacement of the nodes on the surfaces are used to determine the damage initiation and propagation at the interface. The main ingredients of the underlying damage law are exposed below.

Damage initiation criterion. The mechanical behavior of the interface is modeled using a traction-separation law which relates the displacement across the interface to the force vector acting on it. In the absence of any damage, the interface behavior is assumed to be linear with high values of initial interface stiffness (K_i). Linear elastic traction-separation behavior relates normal and shear stresses (t_i) to the normal and shear separation displacements (δ_i) across the interface before the initiation of damage can therefore be described by the following constitutive relationship

$$t = \begin{bmatrix} t_n \\ t_s \\ t_t \end{bmatrix} = \begin{bmatrix} K_n & 0 & 0 \\ 0 & K_s & 0 \\ 0 & 0 & K_t \end{bmatrix} \begin{bmatrix} \delta_n \\ \delta_s \\ \delta_t \end{bmatrix} \quad (28)$$

To predict the onset and development of debonding at the interfaces, a quadratic nominal stress criterion is used (Abaqus® 6.12 Analysis User's Manual, 2014). According to this approach, the damage is assumed to be initiated when the following quadratic interaction function satisfied

$$\left(\frac{\langle t_n \rangle}{t_n^{\max}} \right)^2 + \left(\frac{t_s}{t_s^{\max}} \right)^2 + \left(\frac{t_t}{t_t^{\max}} \right)^2 = 1 \quad (29)$$

where t_i and t_i^{\max} ($i=n,s,t$), are respectively, the nominal traction stresses and the corresponding interfacial strengths in the normal n and shear s and t directions. The Macaulay bracket ($\langle \rangle$) in equation (29) is used to indicate that a pure compressive stress state does not initiate damage at the interface.

Energy-based damage evolution law. For surface-based cohesive behavior, damage evolution describes the degradation of the cohesive stiffness once the initiation criterion is met. Damage evolution is defined here based on the energy that is dissipated as a result of the damage process. An exponential softening law is adopted to model the evolution of the damage variable from damage initiation to final failure. Progression of damage at the interfaces is modeled using the critical mixed mode energy behavior based on the Benzeggagh–Kenane fracture criterion; it is given by

$$G_n^C + (G_s^C - G_n^C) \left(\frac{G_s}{G_T} \right)^\eta = G^C \quad (30)$$

where $G_S = G_s + G_t$, $G_T = G_n + G_s$, the quantities G_n^C , G_s^C , and G_t^C refer to the critical fracture energies required to cause failure in the normal, first, and second shear directions, respectively. G^C refers to the total critical mixed-mode fracture energy, and G_n , G_s , and G_t represent the work done by the normal and the first and the second shear forces acting in the interface, respectively, and η is a cohesive property parameter.

Indeed, the simulation of ballistic impact behavior of hybrid ceramic/FRP composite materials is a complicated aspect because of several reasons such as the anisotropic properties of composites, the nonlinear material behavior, the complex damage mechanisms of both ceramic and composite materials, and the interaction behavior between the adjacent surfaces. Consequently, a universal numerical approach is required to be developed, so that the ballistic impact response of ceramic/composite can be assessed by considering all of the above factors simultaneously. The strategy of

structure used in the numerical simulations and parametric analyses in ‘Results and discussion’ section consists of a projectile having a cylindrical shape with a diameter of 16.5 mm, a length of 32 mm and a mass of 11 g, a strike-face plate of ceramic (150 mm × 100 mm × 10 mm), and a WFRP composite backing laminate (150 mm × 100 mm × 4.8 mm), as shown in Figure 2(b).

The ceramic material used in this study is alumina with purity of 99.5%, for which the Johnson–Holmquist (JH-2) constitutive relation and damage criterion exposed in ‘Constitutive relations and failure models’ section are adopted. The associated material parameters for the JH-2 material behavior are taken from (Rashed et al., 2016) and tabulated in Table 1.

In the ballistic analysis, two different materials of WFRP composite backing laminate are employed, namely: carbon fiber fabric/epoxy and glass fabric/epoxy. The numerical implementation of the constitutive model presented in ‘Constitutive relations and failure models’ section for these materials requires the following material input parameters: the elastic material constants, damage initiation and damage evolution coefficients, and shear plasticity coefficients.

The elastic material constants include the Young’s moduli in the fiber directions (E_1 , E_2), the Poisson’s ratio (ν_{12}), and the shear modulus (G_{12}). The damage initiation parameters are defined by the tensile and compressive strengths along the fiber directions (X_{1+} , X_{1-} , X_{2+} , X_{2-}) and the in-plane shear stress at the onset of shear damage (S_{12}). On the other hand, the damage evolution parameters are obtained from the tensile and compressive fracture energies per unit area along the fiber directions (G_f^{1+} , G_f^{1-} , G_f^{2+} , G_f^{2-}) and by the parameters α_{12} and d_{12}^{\max} (maximum shear damage) given in equation (27). The shear plasticity coefficients include the initial effective shear yield stress, $\sim\sigma_{y,0}$, and the coefficients C and γ in the hardening function in equation (22). The material properties adopted for modeling the damage and failure of carbon fabric/epoxy and glass fabric/epoxy plies are given in Table 2 (Chen et al., 2018; Schwab et al., 2016; Schwab et al., 2018).

Table 1. Material parameters for 99.5% purity alumina used in Johnson–Holmquist model.

Parameter	Value
Strength model	
Elastic shear modulus, G (MPa)	1,35,000
Intact strength coefficient, A	0.989
Fracture strength coefficient, B	0.77
Strain rate coefficient, C	0
Fractured strength exponent, M	1
Intact strength exponent, N	0.376
Reference strain rate, $\dot{\epsilon}_0$ (s^{-1})	1
Maximum normalized fractured strength, σ_f^{\max}	0.5
Hugoniot elastic limit, HEL (MPa)	5900
Pressure at Hugoniot elastic limit, P_{HEL} (MPa)	2200
Equation of state	
Density, ρ_0 (kg/m^3)	3800
Elastic bulk modulus, K_1 (MPa)	2,00,000
Second pressure coefficient, K_2 (MPa)	0
Third pressure coefficient K_3 (MPa)	0
Damage model	
Damage coefficient, D_1	0.01
Damage exponent, D_2	1
Bulking factor, β	1

Table 2. Material parameters defining the constitutive behavior of the carbon and glass fabric reinforced epoxy plies.

Parameter	Glass fabric/epoxy	Carbon fabric/epoxy
Density (kg/m^3)	2100	1560
Elastic material constants		
Young's modulus along fiber direction 1, E_1 (GPa)	24	56.813
Young's modulus along fiber direction 1, E_2 (GPa)	24	56.813
Poisson's ratio, ν_{12}	0.108	0.047
Shear modulus, G_{12} (GPa)	4.8	4.206
Damage initiation parameters		
Tensile strength along fiber direction 1, X_{1+} (MPa)	410	802.11
Compressive strength along fiber direction 1, X_{1-} (MPa)	660	707.88
Tensile strength along fiber direction 2, X_{2+} (MPa)	395	802.11
Compressive strength along fiber direction 2, X_{2-} (MPa)	490	707.88
Shear strength S_{12} (MPa)	94	115.8
Damage evolution parameters		
Tensile fracture energy along fiber direction 1, G_f^{1+} (kJ/m^2)	65	44.9
Compressive fracture energy along fiber direction 1, G_f^{1-} (kJ/m^2)	65	39.15
Tensile fracture energy along fiber direction 2, G_f^{2+} (kJ/m^2)	65	44.9
Compressive fracture energy along fiber direction 2, G_f^{2-} (kJ/m^2)	65	39.15
Maximum shear damage, d_{12}^{\max}	1.0	1.0
Shear damage parameter, α_{12}	0.18634	0.18634
Shear plasticity coefficients		
Initial effective shear yield stress, $\tilde{\sigma}_{y0}$ (MPa)	55	55
Hardening function coefficient, C	669.94	669.94
Hardening function exponent, γ	0.823	0.823

Geometrical discretization and boundary conditions

For the implementation of the constitutive behavior of the considered materials, all of deformable parts, including ceramic and composite laminate, are meshed with the reduced-integration linear 8-node hexahedral elements (element type: C3D8R) and 8-node continuum shell elements (element type: SC8R), respectively. Whereas, the projectile is considered as rigid body and is meshed with the discrete rigid element (element type: R3D4).

For the targets on which the simulations and parametric investigation are performed, the ceramic front plate is discretized using 76,800 elements of size ($1.25 \times 1.25 \times 1.25 \text{ mm}^3$) and composite backing laminate with 1,53,600 elements of size ($1.25 \times 1.25 \times 0.3 \text{ mm}^3$). This mesh size is found to achieve a good compromise between accuracy and computational efficiency. Specifically, further refinement in the mesh size is found to have minor or no effects on the numerical values of the results. Furthermore, the underlying composite laminate plate is composed of 16 plies, each one has 0.3 mm thickness and is characterized by a stacking sequence of $[45/-45/0/90/45/-45/0/90]_s$. Each of the 16 fabric plies is individually meshed with continuum shell elements (SC8R). The elements of each ply are regular and oriented according to the fiber orientation. This type of element has the geometry of a 3D solid element, but its kinematic and constitutive behaviors are similar to those of conventional shell elements. In fact, this element type allows for the accurate modeling of stacked composite plies.

The simulation model developed for composite laminate is a more physical approach, closed to the real build up lamination. All laminae are modeled and linked one by one with a zero thickness

cohesive surface. Although, this type of approach is more complex, mainly because the setup of the model is not automated and all have been done manually, it does provide a precise representation of the laminate layup in particular with respect to penalty contact interactions. A 3D model is therefore constructed and the model includes both the whole stacking sequence of laminae and the interfacial damage models presented previously.

For the boundary conditions in all ballistic impact simulations, the four borders of ceramic/composite target are fully fixed to prevent rigid motion of the structure during the impact. The corresponding boundary conditions are formulated as $U_i = 0$ and $UR_i = 0$ ($i = 1, 2, 3$), which respectively represent the translation and rotating degrees of freedom. Initial velocity is assigned to the projectile to initiate the ballistic impact load. To prevent any rigid body modes, the movement of the projectile is restricted along all directions except in the impact direction.

Element deletion scheme

Element deletion is important in ballistic impact simulations to prevent excessive distortion of the elements, which can cause the simulation to terminate prematurely. Without an element removal scheme, the elements will continue to deform until excessive distortion of fully damaged elements cause instability in the model during explicit integration. Moreover, the element deletion criteria are substantial for accurate computation of stress field and to ensure the correct simulation of the kinematics of ballistic impact process from damage initiation to complete penetration. The element removal criteria used in this work for ceramic and composite materials are similar to those used in Liu et al. (2016) and Schwab and Pettermann (2016), respectively.

Within the JH-2 failure model of ceramic, fracture takes place when either damage reaches a critical value of 1.0 or when negative pressure reaches a value of maximum tensile pressure of 330 MPa (Naik et al., 2013). Thus, the element deletions are set into the material model so that the elements are deleted away or eliminated if an element satisfied the criterion. On the other hand, within the composite failure models, damage based element deletion criterion is used along with deformation based deletion criterion to eliminate the fully damaged elements. In the damage based deletion criterion, the elements are deleted when any one tensile/compressive damage variable along the fiber directions 1 and 2 reaches the maximum specified value, d_1 or $d_2 = d_{\max} = 1$. While, in deformation based criterion, the elements are eliminated when the equivalent plastic strain due to shear deformation attains a maximum specified value, $\bar{\epsilon}^p = \bar{\epsilon}_{\max}^p = 0.4$. Therefore, the elements are deleted when any damage or deformation parameter reaches the specified maximum value. In addition, the composite and ceramic fragments produced during the simulation are deleted when they move far away from the impacted zone.

Besides, it should be noted also that in this work the erosion or flattening of the projectile during the perforation is neglected and the mass is maintained constant. This is why the projectile shape is modeled as a cylindrical flat-ended.

Contact and interface properties

During the impact process, the contacts occur between projectile and ceramic, projectile and composite, ceramic and composite, between individual plies of composite laminate, and between the newly created fragmented surfaces (pieces). A general contact algorithm available in ABAQUS/Explicit is therefore used to model all these contact scenarios in order to prevent element interpenetration. It is implemented using the penalty and “hard” contact formulation methods in the entire interaction calculation. Since the contact surfaces normally transmit shear or normal forces, prescribing a friction that defines the force in resisting contact surfaces is necessary. In our work the

friction coefficients are defined among all contact surfaces of the simulation model. Based on the data available in the literature, the coefficient of friction between fabric plies is set as 0.3, while between projectile-ceramic and ceramic-composite surfaces is considered as 0.28.

Meanwhile, to simulate the interface delamination that could occur within the composite plies and between the composite and ceramic, additional cohesive contact based on the CZM ('Constitutive relations and failure models' section) is adopted to predict the damage initiation and growth of delamination. The material parameters defining the constitutive response of the interface between fabric plies used in the present work are taken from (Schwab et al., 2018; Schwab et al., 2016) and listed in Table 3.

A thin adhesive layer is in addition required to bond the ceramic front plate to the underlying composite back-up laminates. As far as the adhesive layer is concerned, it is assumed to be made of epoxy resin material. For modeling the cohesive behavior in the epoxy resin layer, surface-based cohesive contact formulation is adopted as in the case of composite plies. The thickness of the resin at the interface is assumed to be small. For such requisitions, cohesive elements with zero thickness or a surface-based interaction can be utilized to model the epoxy behavior. Cohesive element method often requires a fine mesh and this negatively affects the critical time step. Therefore, the surface-based contact approach that follows a similar constitutive behavior as cohesive element is presently used to describe the adhesive interface between the ceramic and the composite. The cohesive contact model parameters for epoxy are presented in Table 3 (Mousavi and Khoramishad, 2019). In addition, the cohesive property coefficient (η) in equation (30) is adopted as 1.2, 1.45, and 1.8 for epoxy, carbon fabric/epoxy, and glass fabric/epoxy, respectively.

So far, all what related to the formulation of the finite element model, computational procedure and associated material parameters related to the problem of ballistic impact have been profoundly described.

Validation of FE model

The predictive capability of the proposed FE model is assessed through comparisons with the impact experiments reported in Hetherington and Rajagopalan (1991) and the analytical model in Naik et al. (2013). The assessment is made on the basis of residual velocity of the projectile after the impact against the ceramic/composite target. To perform the validation, three different

Table 3. Interface properties determining the initial stiffness of the interface, damage initiation and evolution of the simulated materials.

	Mode I	Mode II	Mode III
Glass fabric/epoxy			
Interface initial stiffnesses, K_i (N/mm ³)	10 ⁶	10 ⁶	10 ⁶
Interfacial strengths, τ_i^{\max} (MPa)	35.07	68	68
Critical energy release rates, G_i^C (N/mm)	1.21	4.55	4.55
Carbon fabric/epoxy			
Interface initial stiffnesses, K_i (N/mm ³)	10 ⁶	10 ⁶	10 ⁶
Interfacial strengths, τ_i^{\max} (MPa)	60	79.289	79.289
Critical energy release rates, G_i^C (N/mm)	0.9	2.0	2.0
Epoxy			
Interface initial stiffnesses, K_i (N/mm ³)	10 ⁶	10 ⁶	10 ⁶
Interfacial strengths, τ_i^{\max} (MPa)	30	80	80
Critical energy release rates, G_i^C (N/mm)	0.52	0.97	0.97

ceramic/glass WFRP composite targets are constructed with dimensions of 150×150 mm and with different combinations of thicknesses of ceramic as listed in Table 4. A flat-ended cylindrical projectile with diameter of 12.7 mm and mass of 46.8 g is considered. The ceramic plate and composite plies are discretized with an element dimension of $1 \text{ mm} \times 1 \text{ mm}$. The specification and mechanical properties of the ceramic, composite backing plate and interfaces used for the current validations are given in Tables 1–3. The simulation results of the residual velocities are presented in Table 4 and compared with experimental measurements and analytical prediction. A very good agreement is obtained between the FE model and the results of experiments as well as from analytical predictions over the pertinent range of impact velocities. These comparisons provide validation of the present FE model before it is used in the ensuing numerical simulations and parametric analyses. Furthermore, in Figure 3 the deformation of ceramic and composite materials is displayed after complete penetration of the impacted targets used to validate the developed FE model.

In the next section, we aim to perform numerical simulations to comprehensively investigate the damage and energy absorbing mechanisms of the underlying hybrid ceramic/composite systems during the ballistic impact process.

Results and discussion

Numerical simulations of ballistic impacts are performed to comprehensively investigate the damage behaviors of ceramic/composite materials caused by the ballistic impacts. The ballistic impacts are implemented with various impact energies and the impact responses are characterized based on the history curves of residual velocity, impact force and energy dissipated as well as the retrieved damage patterns and projected cohesive damage (delamination) areas of adhesive layers at ceramic/laminate interface and at interfaces between laminate plies. In addition, a parametric study on the influence of interface properties and friction coefficients on the projectile residual velocity is performed.

Ceramic/composite performance

In this section, the performance of the ceramic/composite target displayed in Figure 2 under impact of rigid projectile is investigated. Three instantaneous ballistic impact velocities of 400, 600 and 800 m/s are assigned to the cylindrical projectile to obtain the impact energies of 880, 1980 and 3520 J, respectively. History curves of projectile impact force and projectile residual velocity of alumina/glass WFRP composite during ballistic impacts with various impact energies are depicted in Figures 4 and 5, respectively. The ballistic impact response and damage process are well captured during numerical simulations. As illustrated in Figure 4, the impact force rises steadily with the

Table 4. Comparison of the residual velocity obtained with present model and with experimental and analytical predictions.

Ceramic thickness (mm)	Composite backup thickness (mm)	Impact velocity (m/s)	Residual velocity (m/s)		
			FE model (present)	Experimental Hetherington and Rajagopalan (1991)	analytical Naik et al. (2013)
4	5	893	817	832	850.6
6	5	880	798	800	818.3
9	5	898	739	693	793.8



Figure 3. The deformation of ceramic and composite material of the impacted targets used in the validation. (a) Ceramic 4 mm, composite 5 mm (b) Ceramic 6 mm, composite 5 mm (c) Ceramic 9 mm, composite 5 mm.

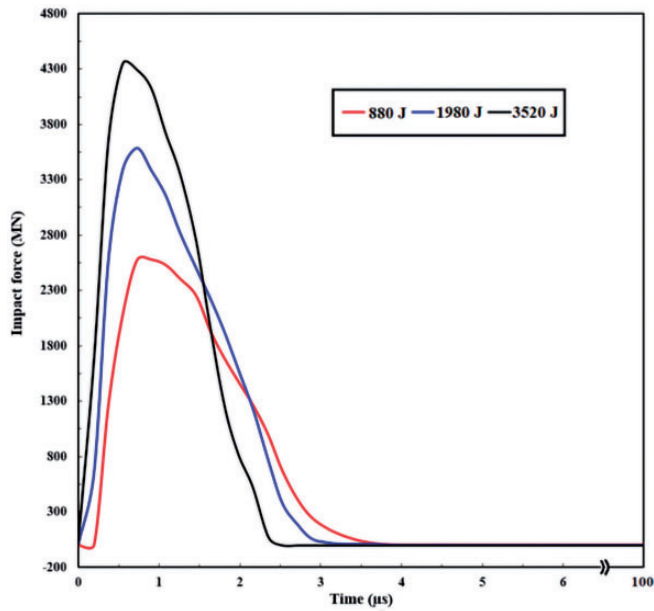


Figure 4. Impact force histories of the projectile impacting the alumina/glass WFRP at initial strike velocities of 400, 600 and 800 m/s.

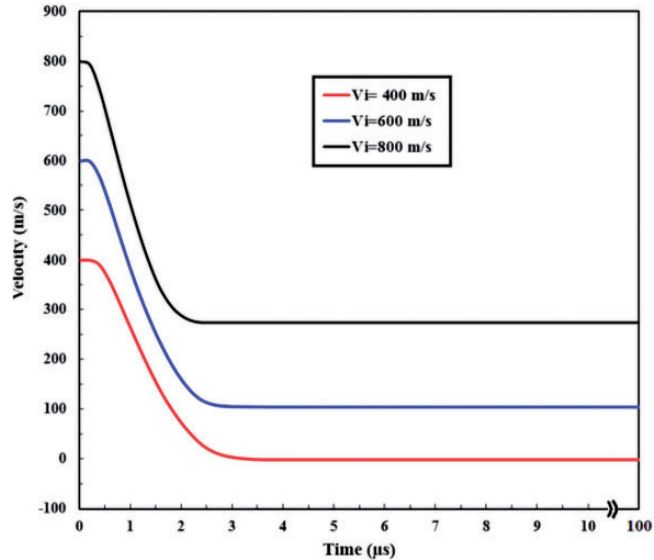


Figure 5. Velocity history curves of the projectile during the ballistic impact of alumina/glass WFRP at initial strike velocities of 400, 600 and 800 m/s.

increase of ballistic impact energy. Besides, the impact force peaks and the drops of force are observed. The force drops occurring immediately after the peaks could correspond to the initiation of failure in the alumina front layer as well as the initiation of damage at the interface between the alumina layer and laminate.

Also it is obvious that upon the impact of projectile on alumina/glass composite, the force of projectile increases sharply and then decreases during the penetration process. The onset of impacts occurs nearly at the same time, then the impact forces begin to increase. After the forces reach the maximum values (at times of $0.74 \mu\text{s}$, $0.73 \mu\text{s}$ and $0.55 \mu\text{s}$), they rapidly descend back to zero at different times of $3.78 \mu\text{s}$, $3.40 \mu\text{s}$ and $2.53 \mu\text{s}$ for the impact energies of 880, 1980 and 3520 J, respectively. This means that the initial impact energy in each loading case is significantly diverse, and the final dissipated energy reaches the converged value at different time for each impact scenario.

The variation of the projectile residual velocity versus time for the three impact scenarios is displayed in Figure 5. As shown, at initial velocity of 400 m/s the projectile cannot perforate the alumina/glass target. The projectile decelerates during impact until its velocity becomes zero at about $3.5 \mu\text{s}$, and then accelerates to a constant negative value of -2.3 m/s after rebounding from the target. Therefore, the ballistic limit velocity or the minimum velocity of projectile for perforation the ceramic/glass target is almost 400 m/s. Under an impact velocity of 600 m/s, it can be clearly seen that the velocity of the projectile decreases during impact and at $3.30 \mu\text{s}$ the velocity of the projectile starts to become stable (104.5 m/s), which is due to the full penetration of the projectile into the target. In addition, at initial velocity of 800 m/s, it can be observed that the projectile decelerates during impact and then maintains a constant velocity of 273.5 m/s (at time = $2.5 \mu\text{s}$) after perforating the target.

With respect to the backing laminate made of carbon WFRP composite and based on its material parameters given in Table 3, a similar behavior is indeed found. When the alumina/carbon target is

impacted with the three initial velocities as in the case of glass composite backing, very slight increases in the residual velocities are obtained compared to the glass backing ones. Therefore, from here onwards we will focus on the glass composite backing type.

Damage mechanisms of ceramic/composite target

Although the residual velocity and impact force of the projectile indicate the ballistic performance of the target, the qualitative illustration of fracture mechanism will not be achieved by these quantitative values. For better and clear understanding of fracture propagation in ceramic/composite target, the damage and pressure contours of the ceramic/composite target at different time steps after projectile impact will be investigated in the sequel.

Figure 6(a) to(c) show the deformation of alumina/composite target during ballistic impact event at three different initial strike velocities. When the projectile impacts the target, the alumina/composite target provides resistance for the penetration of the projectile into the target. In the first phase, which begins upon impact, damage is initiated from both the front and back surfaces of ceramic, producing a cone crack in the alumina ceramic front advancing in impact direction. During this phase, the projectile is unable to penetrate the alumina, because the damage region is below a critical size, consequently the projectile velocity decreases rapidly. On the front surface of ceramic, damage is caused due to the great pressure generated by the impact contact of the projectile. On the back surface of alumina ceramic, damage is caused by tensile wave reflected from the interface between ceramic and composite back laminate. Damage on the back surface then rapidly propagates towards the front surface, and this leads to the failure of most ceramic below the projectile, and as a result the projectile is initiated to penetrate.

Afterwards, due to the progress of the projectile and high compressive stress, a conical crack is developed towards the back surface of alumina, and the extent of damage on the back surface is increased. When the cone crack reached the back surface, a fragmented alumina conoid will be formed. Because the fragmented conoid is still supported by the composite backing laminate, this helps to redistribute the impact load to a larger area of the back laminate surface. Eventually, the projectile and fractured alumina conoid cause the deflection of composite layers and the remaining kinetic energy of projectile is absorbed by the kinetic and strain energy of both alumina conoid and woven composite backing layers. Based on the initial strike velocity, the fracture of lamina fibers or matrix may occur and the projectile can perforate the back-up composite laminate. As shown in Figure 6(b) and (c), the target is perforated by the projectile at impact velocities of 600 m/s and 800 m/s, and both the fragmented alumina conoid and fractured composite layers move forward as an agglomeration. However, at impact velocity of 400 m/s (Figure 6(a)), the target is not perforated even though the alumina/composite layers are almost pierced through its thickness. In this case, the projectile is intercepted and bounced back with low velocity, implying that 400 m/s is close to ballistic limit of the underlying alumina/composite target. It should also be noted that at this velocity, the projectile is remained in the fragmented alumina for long time causing an increase in deflection and subsequently fracture of composite backing material and eventually the damaged material moves ahead of the projectile.

When the impact behavior of the composite backing laminate is examined, it can be seen that the damage and failure mechanisms at the end of impact event involve spalling and petalling of the laminate as exemplified in Figure 7(a) to (c) at impact velocities of 400, 600 and 800 m/s, respectively. More specifically, in the surrounding area of the formed hole, material spalling and petalling flower-like created by the projectile can be observed on the back side in the last few plies of the laminate as shown in Figure 7. In addition, increasing the impact velocity results

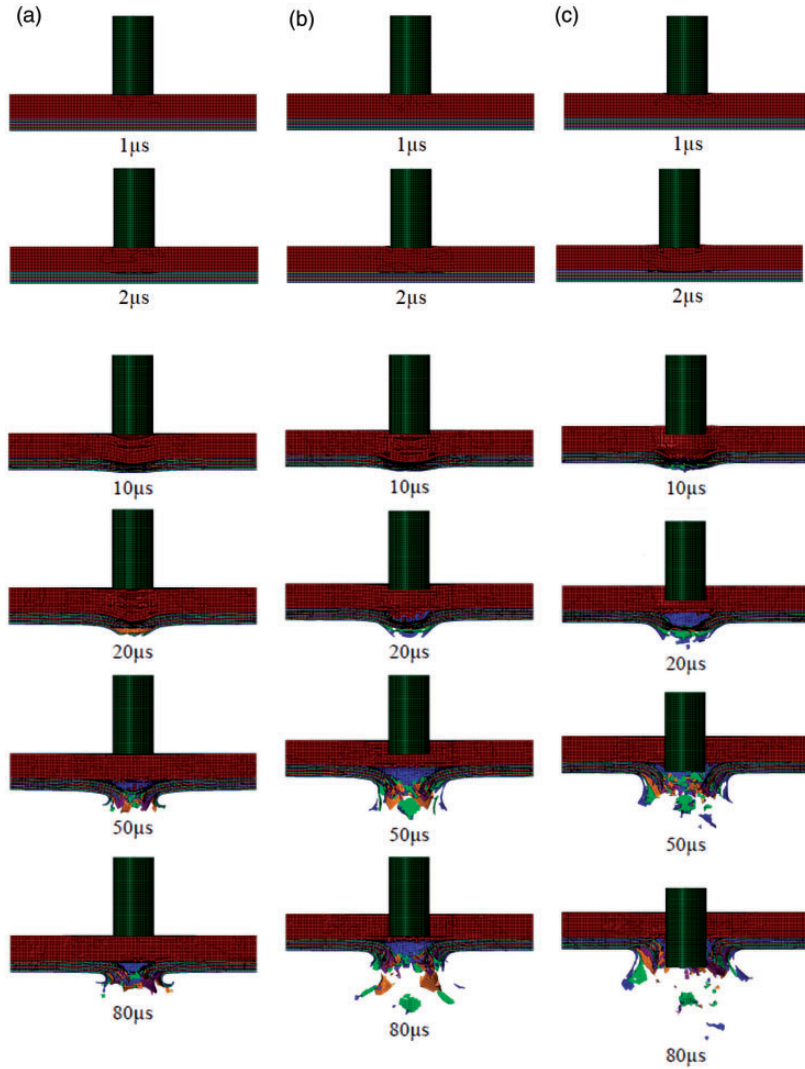


Figure 6. Temporal evolution of material deformation status in the alumina-hard face/glass composite backing laminate target at three projectile initial velocities (a) 400, (b) 600 and (c) 800 m/s.

in highly localized damage in the laminate with a clearly visible hole as a result of perforation. The hole sizes do vary in each ply, resulting in a large hole diameter laminate with increased the impact velocity (see Figure 7).

Furthermore, of particular interest for better understanding the role of the alumina hard-face and the composite backing layers in the overall ballistic performance of the hybrid target, is the exploring the evolution of the pressure status within the target. As shown in Figure 8(a) and (b), the ceramic material directly below the projectile tip and in the surrounding region are under compression along thickness direction. As the projectile impacts the target, longitudinal and shear stress waves are generated and travel through the thickness from the front to the back face. At the early

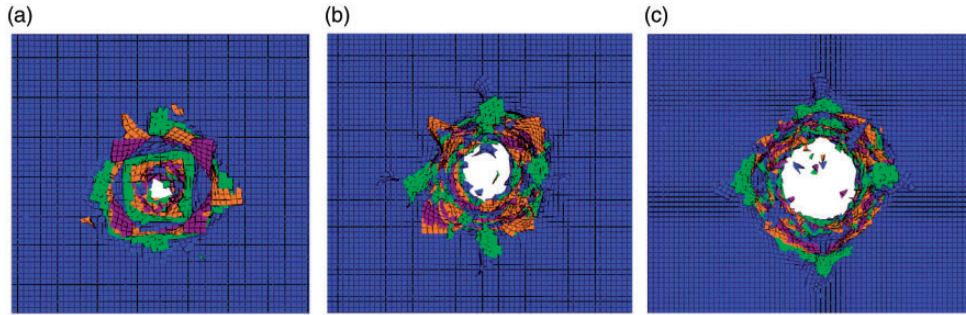


Figure 7. Back view illustrating the damage morphology of the rear side around the created hole at impact velocity of (a) 400, (b) 600 and (c) 800 m/s.

stage of the ballistic impact event, the mechanical response of the hybrid ceramic/composite and of the projectile is governed by the ceramic hard-face layer of the target. At this stage, the pressure field in the target is dominated by a shock wave emanating radially from the location of impact. As the time progresses, the stress wave propagates further and when the impulse/shock wave reaches the ceramic/composite laminate interface, a negative pressure zone begins to develop at the rear face of the ceramic layer. Due to the weak ability of the alumina ceramic layer to support tension loads, the region subjected to the negative pressure will experience a brittle failure in tension. Within the composite laminate, a zone subjected to negative pressure is also observed. In conjunction, the failure status of the alumina/composite materials is dominated by the damage caused by compression of alumina plate along thickness direction, radial and transverse cracking in alumina layer, shear plugging and pulverization of alumina. Possible additional damage mechanisms are also compression of composite backing plate, tension in the woven yarns, cohesive damage and matrix cracking. In the late stages of the impact process, when the projectile penetrates more, considerably larger regions of alumina and composite are subjected to both the negative pressure and positive pressure. Accordingly, a larger region of the target structurally fails either through pulverizing due to compression and/or tensile failure due to the negative pressure. Composite failure in the final stage appears to be dominated by the spalling and petalling of composite backing laminate with plug formation; the detailed damage mechanisms of the composite backing layers will be thoroughly covered later on.

Damage development in the alumina ceramic layer

In order to further reveal the damage mechanism of the underlying ceramic/composite target, we intentionally analyze the damage patterns retrieved from the models on the impacted and back side of the alumina layer during the ballistic impact process. Figure 9(a) and (b) show the produced damage in the alumina layer at three impact velocities of 400, 600 and 800 m/s at times of 10 and 80 μ s, respectively. The letters “F” and “B” in the alumina layer identification indicate front and back surface, respectively, while the number indicates the initial impact velocity. It is evident from Figure 9 that the impact damage is located in the vicinity of the impacted zone and the damage is spread out to a larger area on ceramic front side after impact compared to the rear side. Another observation is that, at early stage of impact, the density of cracks is much higher beneath the impact zone in both front and back sides, thus, a higher number of incipient fragments are developed.

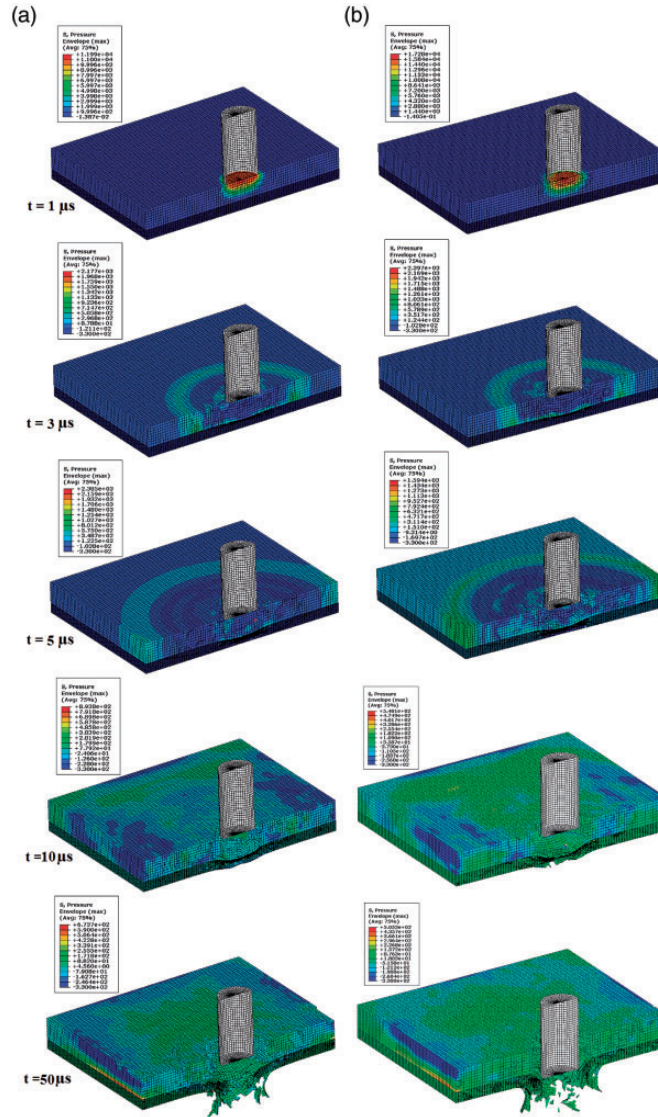


Figure 8. Temporal evolution of pressure status in the alumina/composite target at two projectile initial velocities (a) 600 and (b) 800 m/s.

Besides, the damage area on the back side is generally localized around the projectile impact point with perforation diameter relatively larger at a high velocity of 800 m/s compared consecutively to the velocities of 600 m/s and 400 m/s (Figure 9). As seen in Figure 9, two main damage mechanisms can be observed: radial cracks and cone cracks. The radial cracks are observed to extend from the impact point on the back side and outward in a radial direction. At velocity of 400 m/s and time step 80 μ s, the damage on the back face is primarily radial cracks and at a higher velocity, connecting or rather discontinuous hoop cracks appear to intersect a number of radial cracks. The cone cracks are best perceived in the cross-sectional view as previously illustrated in

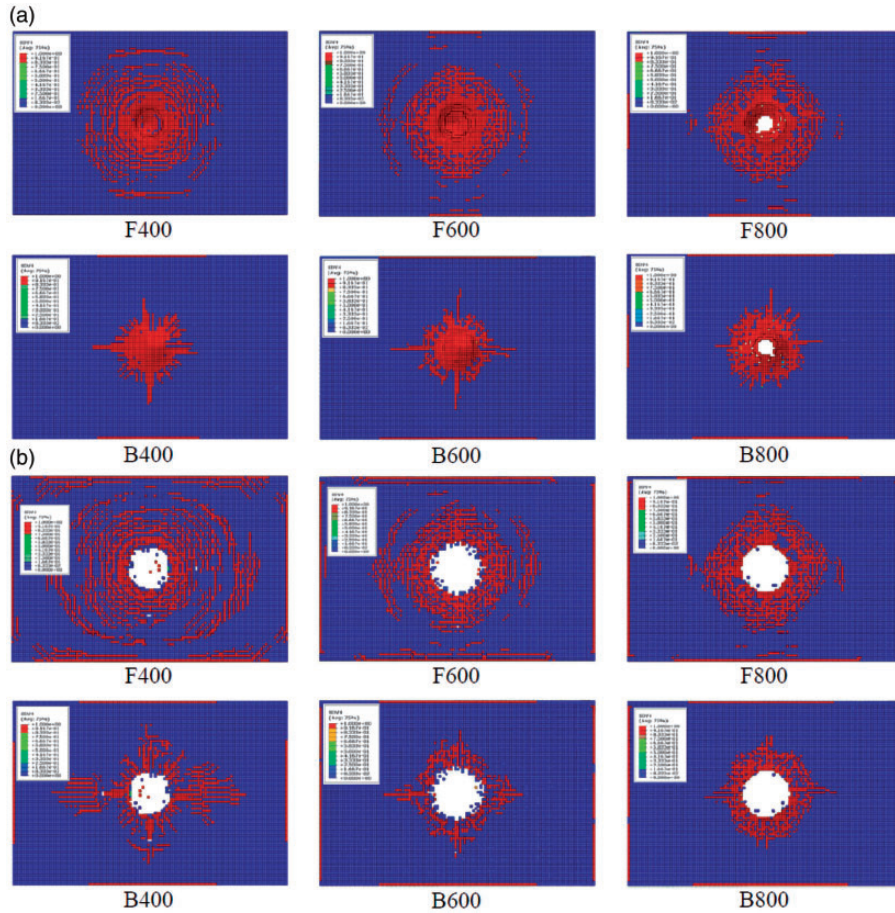


Figure 9. Damage patterns developed on the front and back sides of alumina ceramic layer at (a) 10 and (b) 80 μ s. SDV4 stands for the damage variable D ($D = 0$ intact state and $D = 1$ damage state).

Figures 6 and 8, where they are observed to form a cone extending from the impact point on the front surface and spread to the back face through the entire thickness of the alumina.

With regard to the damage at the edges, it can be seen that the surface waves produced by the impact can slightly damage the edges of the alumina ceramic layer under fully fixed constraint (see Figure 9(b)). Although it occurs slightly, the change of the boundary conditions from fully clamped to a clamped free (two opposite edges clamped and two free) is found to effect the damage produced at edges of the ceramic plate. For the clamped free boundary condition, no damage is observed at the two free edges of the plate, whereas it is observed at the clamped edges.

Damage mechanisms of composite backing laminate

Qualitative aspects such as the shape and degree of the damaged zone in the composite backing laminate subjected to ballistic impact are considered in the sequel. Overall, the composite laminate exhibits a complicated damage and failure behavior with various modes of failure, such as fiber

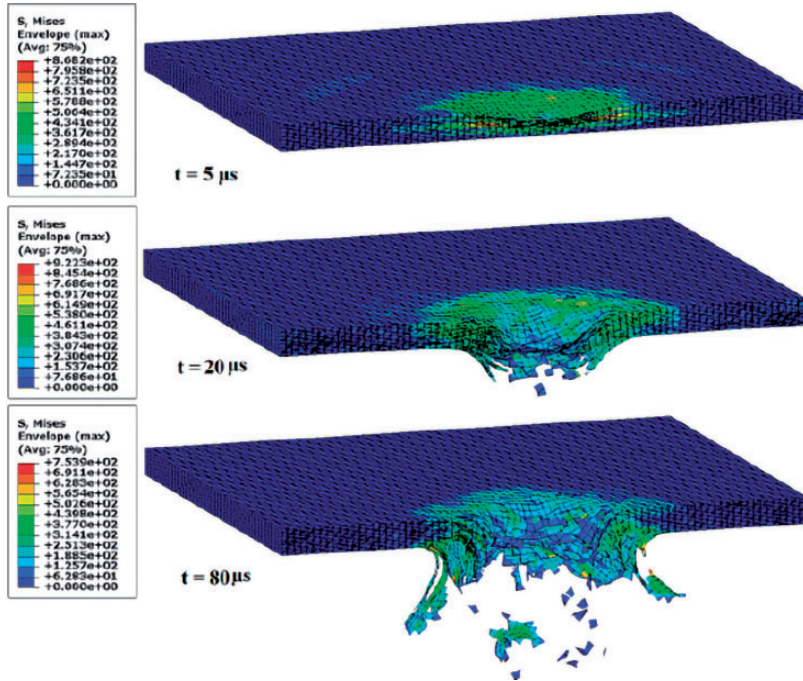


Figure 10. Cross-sectional perspective illustrating the von Mises stress contour of composite backing laminate.

breakage, matrix cracking, matrix plasticity and delamination of plies. All of these damage mechanisms are likely occurring during ballistic impact. It is therefore convenient to describe the damage modes retrieved in the composite during impact of the underlying alumina/composite target, using the damage variables presented in ‘Fabric reinforced composites constitutive model’ section.

A cross-sectional view of the damage process over increments of time throughout the impact event at 800 m/s (3520 J) can be observed in Figure 10. At the onset, it can be seen from Figure 10 that the stress concentration is very intense around the impact zone of the front faces, resulting in a sequence of compression and shearing forces along the interfaces between the plies. Afterwards, the impact force travels down to the bottom through the laminate thickness, contributing to large deformations in these areas. When the fibers reach their tensile/compressive resistive tolerance this leads to fractures along the woven fabric directions. Along with fiber breakage and perhaps also shear matrix cracking inside the composite laminate, the interlaminar delamination can be considered as the driving force that causes several pieces of the plies to pull out ahead of others and then are fractured due to the stretching force emanating from the projectile. This in turn leads the entire composite layers to completely fractured around the impact zone and subsequently perforated at end of the impact process (at $t = 80 \mu\text{s}$) as depicted in Figure 10.

In sum, it can be viewed that the present stress concentration areas in each ply in the laminate are susceptible to damage.

To have a brief view of the damage evolution variables, the tensile damage (d_{1+} , d_{2+}), compressive damage (d_{1-} , d_{2-}), shear damage (d_{12}) and matrix plasticity due to shear in all layers of the composite laminate are depicted in Figure 11. The fully failed materials are deleted from the model according to element removal strategy exposed in ‘Element deletion scheme’ section and the red color in each layer indicates the higher damage level while blue represents intact material as shown

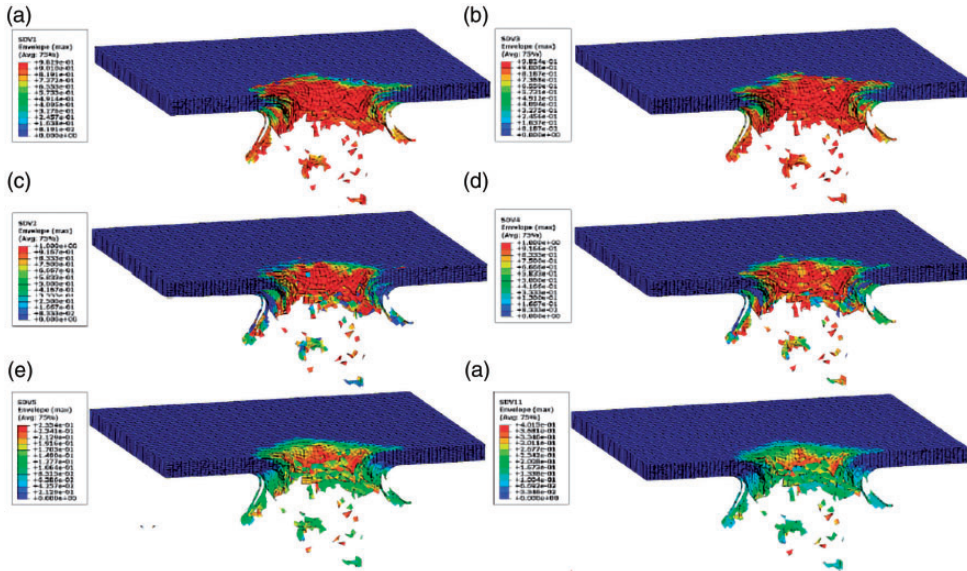


Figure 11. Patterns of damage variables with respect to (a) fiber tension along fiber direction-1 (d_{1+}), (b) fiber tension along fiber direction-2 (d_{2+}), (c) fiber compression along fiber direction-1 (d_{1-}), (d) fiber compression along fiber direction-2 (d_{2-}), (e) shear damage (d_{12}) and (f) matrix plasticity for all composite layers at the end of the impact process at 3520 J impact energy.

in the Figure 11. With regard to the final damage patterns in the entire laminate, it is of great interest to observe from Figure 11 that the damage variables $0 < d_{i\pm} < 1$ in fiber directions 1 and 2 occur rather locally around the impact zone. Similar information is also obtained for other damage mechanisms but their severity is less. In general, It is apparent from damage contour plots that all damage mechanisms occur within the composite laminate, with fiber tensile damage (Figure 11(a) and (b)) is the dominant fiber damage mode compared to fiber compression damage (Figure 11(c) and (d)) while the matrix shear failure mode appears to be less important since $0 < d_{12} < 1$ does not exceed 0.25 (Figure 11 (e)).

To further understand the damage behaviors within the composite laminate, the projected areas of the predicted patterns of the above-mentioned damage variables are plotted for the first and last four plies from their rear side in Figure 12. A few aspects can be discussed for Figure 12. (i) It can be observed that the fully failed damage areas in the back plies are generally larger than the front plies. This can be attributed to the fact that the damage are initiated and developed firstly in the back layers due to the higher developed negative pressure which gives rise to the tensile failure of the back layers first. Also, it is found that the delaminated plies affected by cohesive damage in the back side around the periphery of the projectile are more susceptible to the damage than the front plies. What's more, petalling and material spalling can be seen in the last few plies of the laminate (plies 13-16). (ii) The fiber tension damage degree (1st column) is relatively larger compared to fiber compression damage (2nd column) which possibly due to the larger bending stress. Also, it is found that the damage degree for fiber tension and fiber compression near the impact side is more severe than the non-impact side. (iii) In terms of the tensile damage, it is more likely to occur along the directions that are corresponding to fiber directions. Specifically, the tensile damage values are apparently higher along the corresponding fiber directions, which tend to result in the tensile failure. Regarding

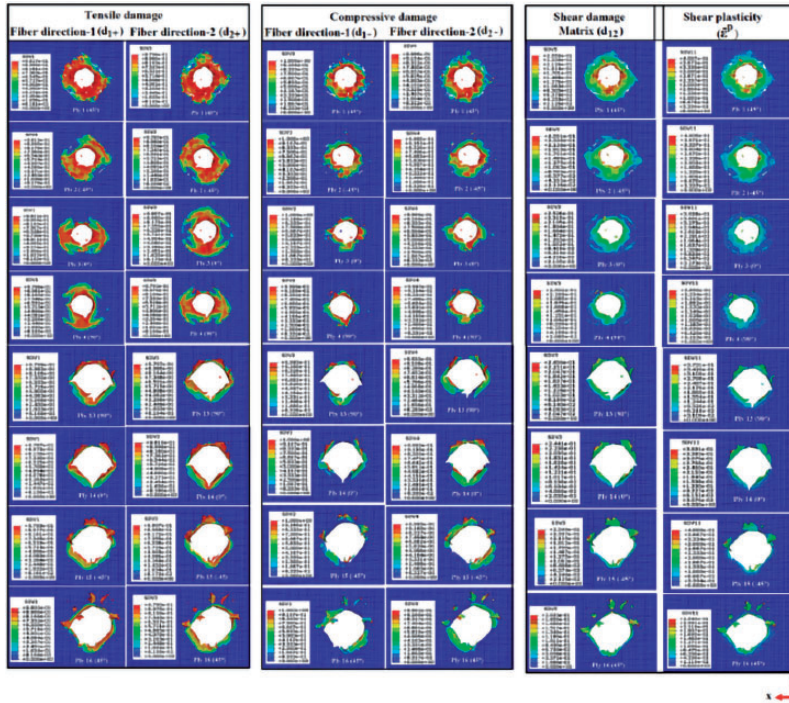


Figure 12. Degree of damage contour for fiber tension, fiber compression, matrix shear and matrix plasticity in the four frontal and rear composite layers [45, -45, 0, 90] at 3520 J impact energy.

the damage degree for shear loading and plasticity of the matrix, it is found that their status variables in each layer are comparatively insignificant as illustrated in the 3rd column, which suggests that they have less effect on the failure of the composite laminate under ballistic impact compared to the other damage modes. Consequently, these observations reveal that the main damage mechanisms arising from the ballistic impact are fiber tensile damage followed by fiber compressive damage and matrix shear damage occurs slightly on the impact surfaces.

Delamination damage mechanism

Herein, the surface based cohesive behavior used to model both the interface debonding between alumina-composite and delamination between individual plies of composite backing laminate, is demonstrated. A detailed comparison of delamination mechanism at different impact energies will also be discussed.

As we explored earlier, the damage initiation criterion for cohesive surface is based on quadratic stress criterion and the damage evolution is governed by a power law in which the fracture energies for normal and shear modes are specified. The initiation of the damage in the cohesive interaction is obtained by CSQUADSCRT variable (a value of 1 implies initiation of delamination) while damage evolution can be tracked by CSDMG variable. The latter parameter varies from 0 to 1 where 0 means no delamination and 1 indicates complete delamination where the adjacent layers are no longer bonded by the matrix. Figure 13(a) and (b) show the delamination initiation and delamination damage extent patterns through the ceramic/laminate thickness at various time-frames as the projectile passes through

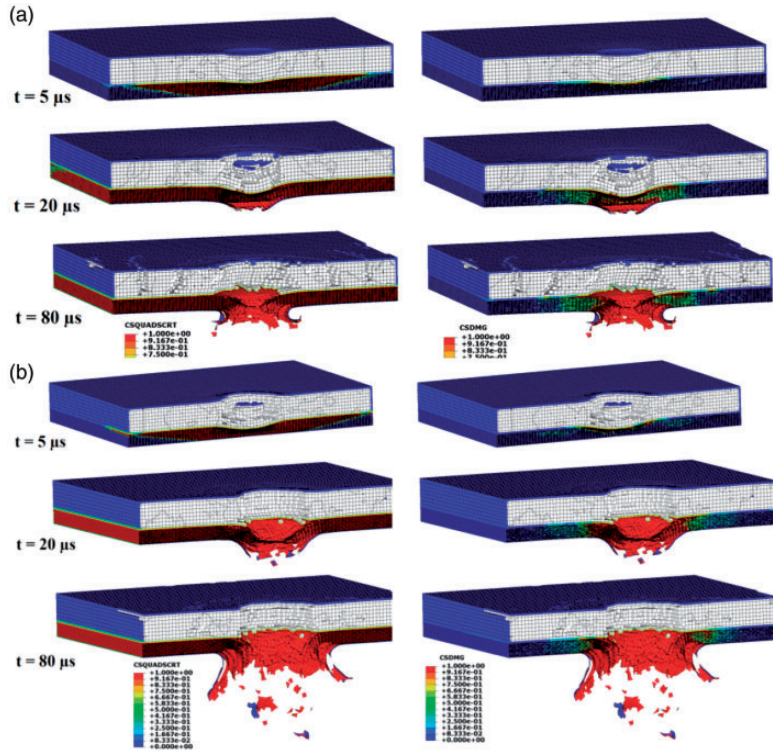


Figure 13. Patterns of delamination initiation and delamination damage extent after (a) 880 and (b) 3520 J impact energy.

the target at 880 and 3520 J impact energies, respectively. As shown in Figure 13, both delamination initiation and delamination damage evolution degree are increasing in size along the direction of the impact as time progresses. Besides, it is remarked that the delamination damage pattern is more conical in shape. In fact, the interface debonding damage results in reducing the bending stiffness of the woven laminate as well as the bending stiffness of adhesive layer between laminate and ceramic by allowing local deformation of the material beneath the projectile and thus diminishing the penetration resistance force. By comparison, the damage area of the interfaces between the alumina layer and the composite laminate is larger than that between composite plies, which may be explained by the difference of adhesion properties between the adjacent layers and because the projectile is first in contact with the interface between the alumina layer and composite laminate.

To observe the variation of delamination damage in the alumina/composite target, the evolution based CSDMG variable is traced for each interface in the target. The delamination profile or rather the projected delaminated area for each interface is shown in Figure 14(a) and (b) at the end of impact by 880 and 3520 J impact energies, respectively. From these figures, we can see that the interface debonding damage mainly occurs at the areas around the projectile impact zone and the delamination damage contour shape is mostly circular for all interfaces. What's more, it is apparent from Figure 14 that the models predict larger areas of delamination at the interfaces close to the impact side of the laminate (Plies 1–4) and relatively smaller areas of delamination at interfaces near the mid-plane and at the back side of the laminate (all areas in red indicate completely delaminated).

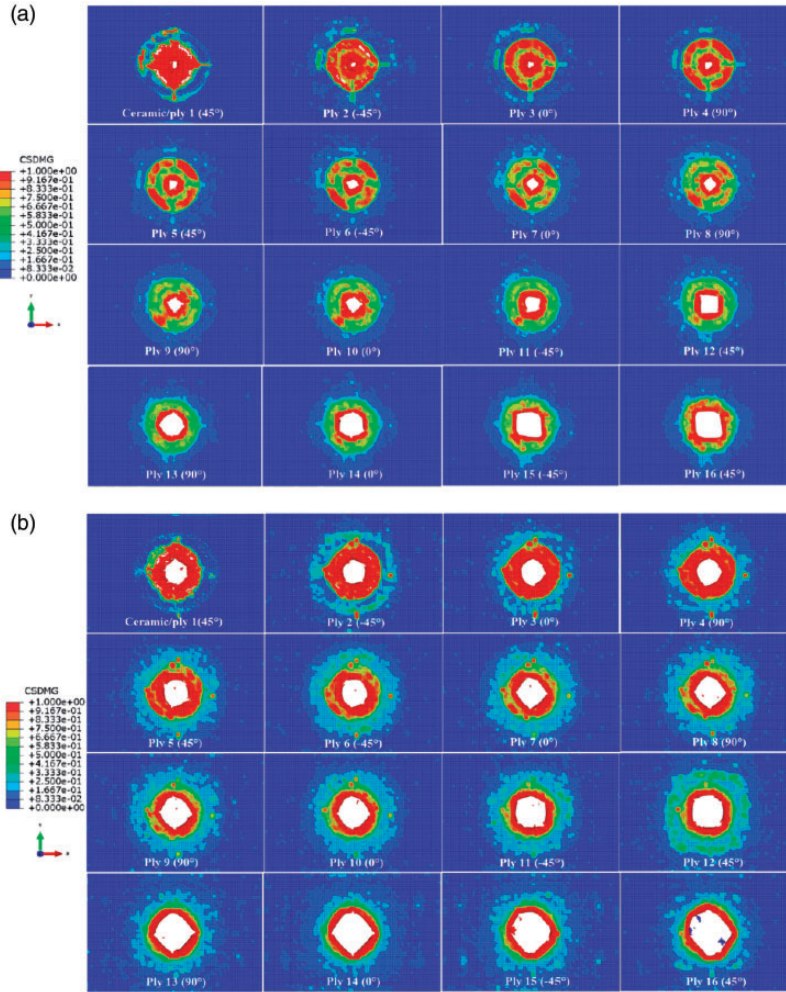


Figure 14. Projected delamination areas obtained at impact energy of (a) 880 and (b) 3520 J. The plies are numbered from impact to back face.

To give insight into the delamination failure mode dependence with the time history, the delamination contours in the top 4 ply interfaces of the laminate are plotted against time of 5, 10, 20 and 50 μ s (see Figure 15). As seen in Figure 15(a) and (b), over the time history, the spread of delamination damage is quite large at impact energy of 3520 J compared to 880 J. The delamination pattern pictured in Figure 15(a) is more oriented along the principal directions of the fibers especially for the 1st interface (alumina/laminate interface) while being fairly circular in the other plies interfaces. At impact energy of 3520 J (Figure 15(b)), it can be seen that the delamination spread shows that the laminae tend to have a preference in growing radially to form a more circular delamination pattern over time.

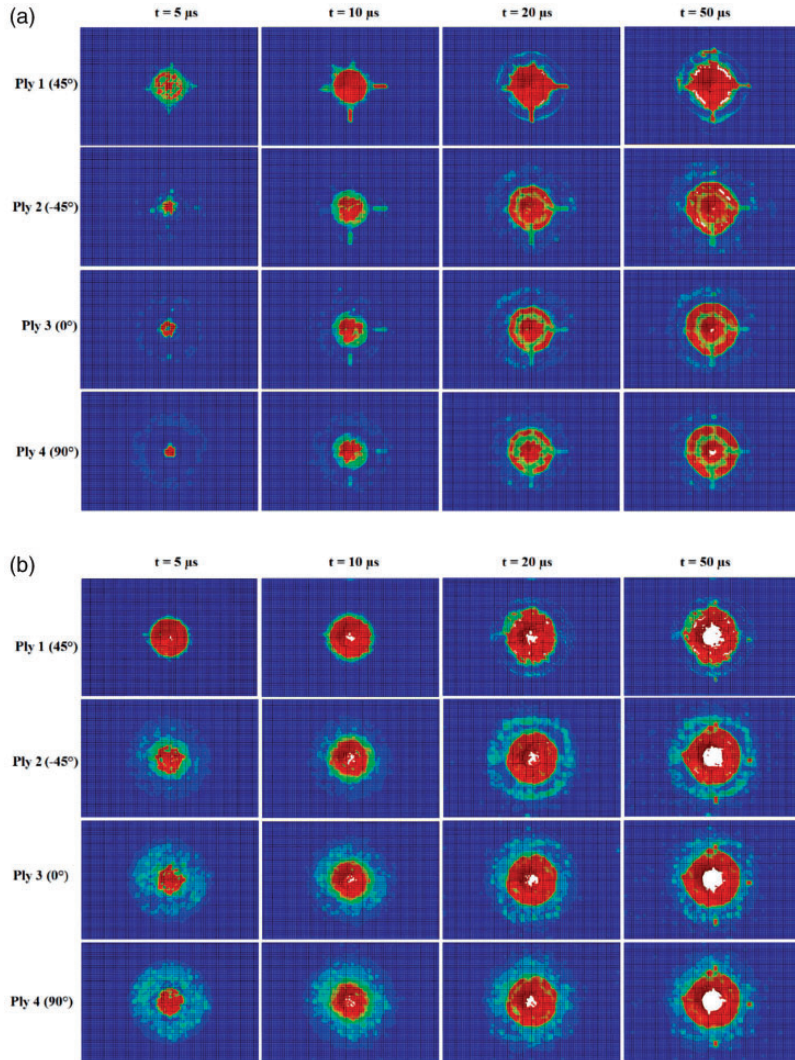


Figure 15. Delamination contour in the top four plies of the laminate versus time after impact energy of (a) 880 and (b) 3520 J.

Energy-based analysis

One of the important outcomes of impact dynamics using a FE simulation code based on an explicit solver is the validation of the energy conservation principle. The numerical simulations will therefore be used to extract further information on the kind and extent of damage modes to determine the major energy absorption mechanisms and then confirm the energy conservation theory. Indeed, simulations will allow to quantify the amount of energy absorbed by various mechanisms such as a) material fracture and fragmentation energy, which includes the energy absorbed by the fiber and matrix damage of composite plies and energy dissipated by ceramic fragmentation; b) interply

energy, which is the energy absorbed by the delamination of fabric layers and debonding between ceramic and composite; c) frictional energy, including friction between the target and the projectile and delaminated layers/fabric debris interactions; and d) artificial strain energy, which is the energy used to suppress the singular modes such as hourglass effects.

In order to confirm the accuracy of the simulations, the typical energy evolution of the entire model shall first be analyzed. According to the total energy conservation principle, the energy-balance equation of the ceramic/composite target-projectile system is given as

$$E_i = \frac{1}{2}m_p V_i^2 = E_{TE}(t) = \frac{1}{2}m_p V_r^2(t) + E_{AB}(t) \quad (31)$$

where E_i is the impact energy (or initial kinetic energy of the projectile), V_i is the projectile impact velocity, m_p corresponds to projectile's mass, $E_{TE}(t)$ is the total energy at time instant t , $V_r(t)$ is the projectile residual velocity, and the term $E_{RKE}(t) = 1/2m_p V_r^2(t)$ corresponds to the projectile residual kinetic energy at time t . $E_{AB}(t)$ in the above equation is the total absorbed energy which can be calculated by

$$E_{AB}(t) = E_{PKE}(t) + E_{IE}(t) + E_{VD}(t) + E_{FD}(t) - E_{PW}(t) \quad (32)$$

wherein $E_{IE}(t)$ can be written explicitly as

$$E_{IE}(t) = E_{SE}(t) + E_{AE}(t) + E_{PD}(t) + E_{DMD}(t) \quad (33)$$

with E_{PKE} the kinetic energy of ceramic/composite panels, E_{IE} the total internal energy, E_{VD} the energy dissipated by viscous effects, E_{FD} energy dissipated through frictional effects, E_{PW} the work done by contact penalties, including general contact and penalty/kinematic contact pairs, E_{SE} the recoverable elastic strain energy, E_{AE} the artificial strain energy, E_{PD} the energy dissipated through inelastic process such as plastic deformation and extensive cracking, and E_{DMD} the dissipation energy due to delamination damage. The total kinetic (E_{TKE}) is the summation of the kinetic energy of the projectile (E_{RKE}) and the kinetic energy due to vibration of both ceramic and composite panels (E_{PKE}).

According to equation (31), the amount of energy absorbed or dissipated by the ceramic/composite panels at any given time t can be calculated using this formula

$$E_{AB}(t) = \frac{1}{2}m_p (V_i^2 - V_r^2(t)) \quad (34)$$

As explained earlier in the previous sections, as lower is the projectile residual velocity, more energy is lost and therefore more resistant is the alumina/composite target. This implies that the target absorbs more energy under various terms of energy absorption mechanisms as illustrated by equation (32). Based on equation (34), the total dissipated energy can be calculated as the difference of the initial kinetic energy and the final kinetic energy of the projectile. Thus, for the three previously applied impact energies of 880, 1980 and 3520 J, the ratios of the total dissipated energy to the initial kinetic energy of the projectile are found to be around 100%, 96.97% and 88.3%, respectively. It is also obviously that more energy is dissipated with the increasing impact energy, such that

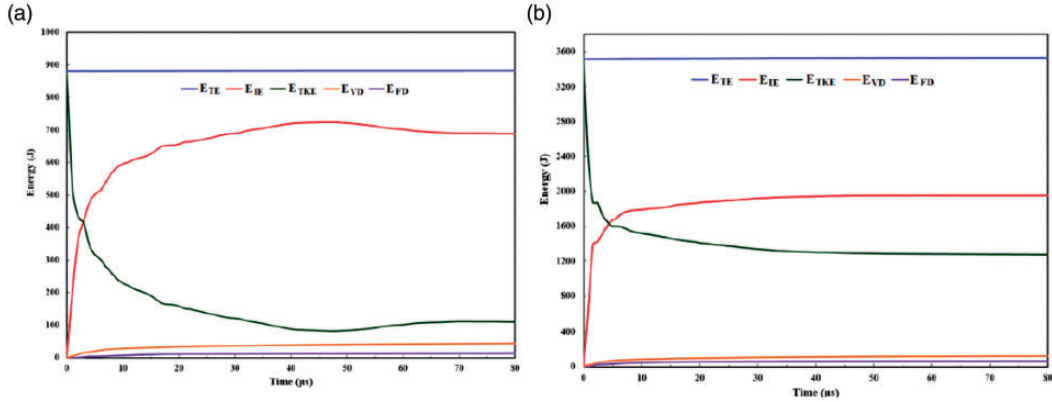


Figure 16. Energy evolution histories under impact energies of (a) 880 and (b) 3520 J.

880, 1920 and 3108.6 J are the energies absorbed when the target is impacted by 880, 1980 and 3520 J, respectively.

The evolution of total energy E_{TE} as well as its associated terms presented in equation (32) are described in Figure 16(a) and (b) at impact energies of 880 and 3520 J, respectively. As shown in Figure 16, at the beginning of the impact, the entire energy is in the form of kinetic energy of the projectile. Later, this energy is split into energy absorbed by various damage mechanisms and the kinetic energy of moving ceramic/composite target and projectile as explained by energy balance equation (equation (31)). It appears also that the total energy (E_{TE}) of the system in the simulation remains constant throughout the analysis for all impact models. In addition, According to the energy relation of the system, it can be observed that at any time step of the simulation, the sum of E_{PKE} , E_{RKE} , E_{IE} , E_{VD} , E_{FD} and less other energy corresponds to the total energy (E_{TE}). This in turn confirms the theory of energy conservation balance in the system and the suitability of the developed models for impact investigation.

Furthermore, it can be clearly seen from Figure 16 that the total kinetic energy of the model (E_{TKE}) decreases substantially as soon as the projectile starts to penetrate into the ceramic/composite target which is due to that an amount of impact kinetic energy is absorbed. This decrease in kinetic energy leads to a slight increase of the other dissipation terms E_{VD} and E_{FD} . On the other hand, the total internal energy of the target (E_{IE}) rapidly increases linearly at the very beginning of impact and then increases gently until becomes almost stable either when the target is completely penetrated by the projectile (Figure 16(b)) or when the projectile is rebounded from the target (Figure 16(a)).

In order to further study the dynamic progressive failure properties for the alumina/composite target, the energy dissipation corresponding to different failure modes is further investigated. Figure 17(a) and (b) exemplify the energy absorbed by each absorption mechanism as a function of contact time for the target at 880 and 3520 J impact energies, respectively. In these figures, the dissipation mechanism of kinetic energy of the ceramic/composite panels due to its vibration (E_{PKE}), the total internal energy (E_{IE}) and its dissipation into E_{PD} , E_{SE} , E_{AE} and E_{DMD} are presented. From the results, it can be seen that during the very initial phase of contact, almost all mechanisms increase with the contact time. After this time, both the elastic strain energy (E_{SE}) and kinetic energy due to panels' vibration (E_{PKE}) gradually decline while the E_{PD} , E_{AE} and E_{DMD} continue to increase. When fully penetrating takes place, all energies remain almost unchanged.

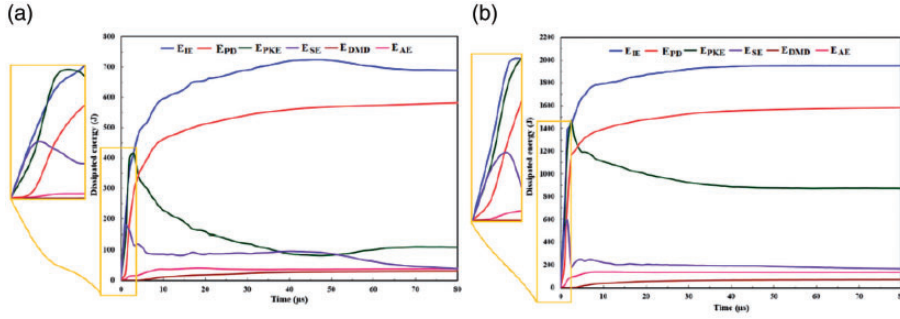


Figure 17. Variation in dissipated energies during the impact process at impact energy of (a) 880 and (b) 3520 J.

Furthermore, the internal energy (E_{IE}) developed due to impact is utilized in general as energy dissipated through inelastic deformation (E_{PD}), elastic strain energy (E_{SE}), dissipation energy due to delamination (E_{DMD}) and artificial strain energy (E_{AE}) in the system, as shown in Figure 17. At low impact energy of 880 J (Figure 17(a)), one can notice that the internal energy (E_{IE}) that develops in the target overlaps with the recoverable elastic strain energy (E_{SE}) during the initial phase of contact. This indicates that in the initial stage of impact process, the developed internal energy dissipates mostly as recoverable elastic strain energy. However, after the development of other damage energies (E_{PD} , E_{AE} and E_{DMD}), the difference between the E_{IE} and E_{SE} becomes explicit. This points out that some of the internal energy that develops in the target is dissipated as damage in the form of failure modes. In opposition, at high impact energies (Figure 17(b)), the overlap with E_{SE} is not observed in the initial phase since the difference between E_{IE} and E_{SE} is evident. Therefore, throughout the simulation time the developed internal energy (E_{IE}) dissipates as a combination of the following elements: E_{PD} , E_{SE} , E_{AE} and E_{DMD} .

Note that for the three impact states, the ratio of permanently absorbed energy due to inelastic deformation (E_{PD}) to the total dissipated energy (E_{AB}) are found to be about 67% and 51% when the target is impacted by 880 and 3520 J, respectively. On the contrary, the contribution in energy absorption by (E_{SE} , E_{AE} and E_{DMD}) is found much less, such that about 13% and 12% of the total dissipated energy at 880 and 3520 J impact energies, respectively. This implies that most of the energy due to ballistic impact is absorbed in the form of inelastic deformation (E_{PD}), with less energy dissipated as elastic energy and delamination (E_{SE} , E_{DMD}). Furthermore, the artificial strain energy (E_{AE}), which is used in the numerical simulation to prevent any hourglass effects, is found to be less than 5% of the total internal energy (E_{IE}) for all modeling impact energies. This value is well acknowledged for not affecting the overall response of the system, and thus confirms that the numerical models give stable solutions.

It is of particular interest now to quantify the contribution of different energy absorbing mechanisms attributed to the alumina frontal layer and composite back panels. Figure 18 graphically summarizes the quantitative contribution of each individual energy absorbing mechanism mentioned in equations (32) and (33). From Figure 18, it is apparent that the absorbed energy by the alumina layer due to inelastic deformation (PD), kinetic energy corresponds to vibration (PKE), energy absorbed due to viscous effects (VD) and artificial strain energy (AE) is, in general, higher than that absorbed by the composite plies. Oppositely, the amount of energy absorbed by composite laminate due to the recoverable elastic strain energy stored in the plies after impact (SE) is found to be large compared to that absorbed by the alumina layer. This energy storage happens as the plies after impact are unable to restore to their original configuration owing to damage inside them.

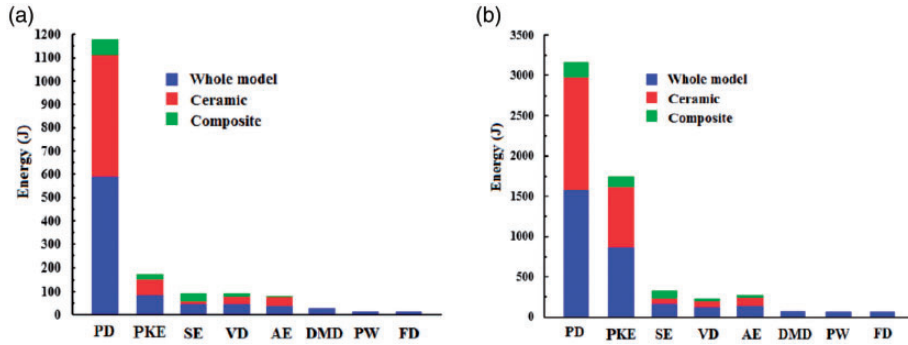


Figure 18. Schematic representation of the contribution of the different energy absorbing mechanisms associated with the alumina layer, composite laminate and whole model: (a) 880 and (b) 3520 J.

By inspection the whole model in Figure 18, it is possible to conclude that the majority part of energy absorption is in the form of inelastic deformation, followed successively by energy absorbed due to vibration, elastic strain energy stored in the panels, viscously dissipated energy, artificial strain energy and less other energies dissipated in the form of delamination, frictional and dissipation by contact penalties. For instance, at high impact energy of 3520 J (Figure 18(b)) the inelastic deformation contributes approximately 51% of the total energy dissipation, kinetic energy of the panels contributes approximately 28%, strain energy contributes 5.4%, viscous dissipation contributes 3.6%, artificial energy contributes 4.2% and the contribution in energy absorption by delamination, friction and contact accounts for 7.8%.

So far, the energetic analysis of the three performed simulations is discussed together with quantitative results confirming the effectiveness of the built models, as regards contact and interaction modeling, ceramic and composite materials behaviors, and element performance.

Sensitivity analysis on some key parameters

Numerical examples will be presented in the following, comprising the sensitivity analysis of some key parameters. We seek to compare the results of considering different friction coefficients and various interface strength and critical energy release rate values on the ballistic response of the underlying alumina/glass WFRP composite target.

Influence of friction. The overall energy dissipated through friction under ballistic impact can be attributed to different phenomena which mainly include lamina-to-lamina interactions, ceramic-to-composite interactions, projectile-to-ceramic interactions, and projectile-to-composite interactions. In order to examine the stability of the model and to understand the effect of friction on the ballistic impact performance, a sensitivity analysis on friction coefficient is performed. The interactions among the projectile and the ceramic/composite materials will be referred as external interactions and its coefficient of friction is symbolized as μf_x while the interactions among the individual composite plies and ceramic-composite surface will be referred as internal or interfacial interactions and its coefficient of friction is represented as μf_i . Initially, it is interesting to conduct simulations with different friction coefficients ranging from $\mu f_i = \mu f_x = 0$ up to 0.9 for the purpose of comparing a frictionless and friction contacts between the adjacent interfaces while impacting the hybrid system with an initial velocity of 600 m/s. The variation of the residual velocity with friction coefficient is shown in Figure 19. According to the results, the friction would significantly affect the

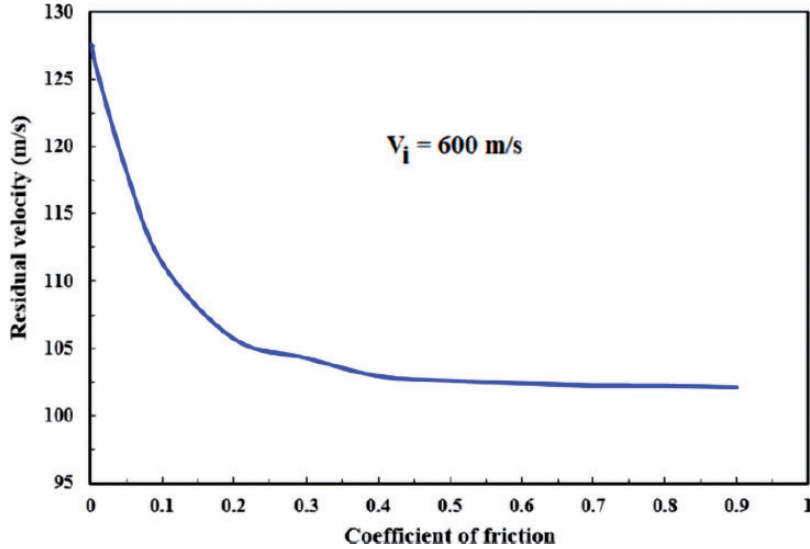


Figure 19. Influence of friction parameter on the projectile residual velocity of ceramic/composite target impacted at 600 m/s.

ballistic behavior of ceramic/composite target. It is found that a lower level of friction results in a higher projectile residual velocity. In the beginning, the residual velocity is observed to rapidly decrease with increasing the friction coefficient, then the velocity starts to become almost stable at coefficient of friction $\mu_f = \mu_x = 0.45$. The reduction percentage of the residual velocity is approximately 20%. Meanwhile, the predicted residual velocity is not sensitive to the friction coefficient greater than 0.5.

In order to distinguish between the influence of friction coefficients of internal and external interactions on the ballistic performance of ceramic/composite, three different values for internal μ_i and external μ_x friction coefficients have been chosen for a total of nine different tests. The projectile velocity history for the nine different cases is illustrated in Figure 20. From this figure, it can be seen that the friction coefficients do not alter the global response of the hybrid structure but rather have a relative impact on ballistic performance. In particular, internal friction corresponding to the ply-to-ply and ceramic-to-composite interactions sounds not to have an effect on the projectile residual velocity if no friction among projectile and ceramic/composite is introduced. However a slight increase on projectile to ceramic/composite friction coefficient leads to some effects in terms of ballistic performance of the target. Moreover, it is noteworthy to notice that within the first 1.5 μs , the effect of friction either internal or external is almost negligible on the ballistic response of the target.

In the meanwhile, it is worth noting that the dissipation energy by friction is still minimal compared to other forms of energy dissipation as illustrated in the previous subsection.

Influence of cohesive interface parameters. A campaign of simulation is carried out in order to assess the influence of cohesive interface parameters on the overall target behavior and then on the amount of dissipated energy due to interlaminar delamination. The main parameters of interest which define interface property are: the interface stiffness (K_i), interface strength (t_i^{max}) and critical energy release rate (G_i^C).

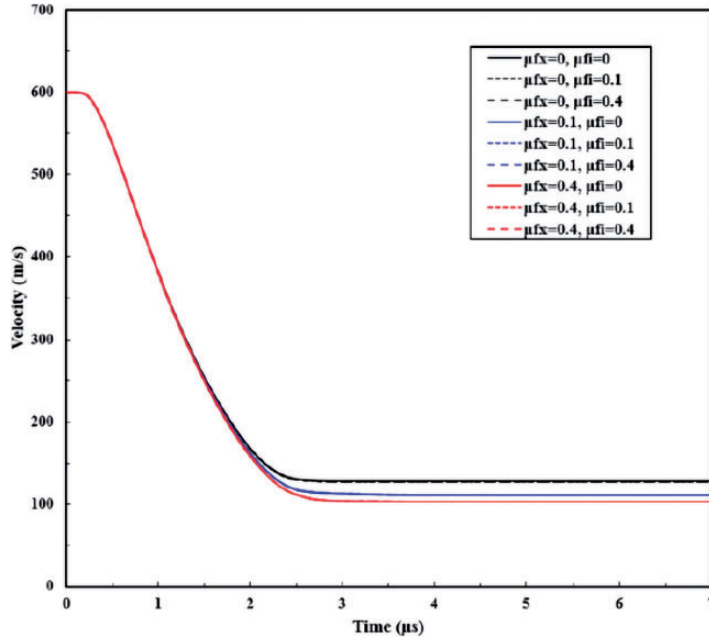


Figure 20. Influence of internal and external friction on ballistic response of the target against 600 m/s incidence velocity.

A parametric study on the cohesive interface properties t_i^{\max} and G_i^C is firstly conducted and the results are shown in Figure 21. Simulation result with the interface properties given in Table 3 is used as the baseline (case 1 in the figure). The values of t_i^{\max} (maximum interlaminar strength mode I, II, III) and G_i^C (critical fracture toughness mode I, II, III) in cases 2 and 3 are increased by 50 and 100%, respectively. In cases 4 and 5, the values of t_i^{\max} and G_i^C are decreased by 50 and 80%, respectively. From the history curve of total kinetic energy (kinetic energy of the projectile and target panels) depicted in Figure 21(a), it is found that the kinetic energy is relatively insensitive to the increase of both interface strength and fracture toughness values. Actually, the same trend is also observed for the dissipated energy by delamination damage; in general, the results are not sensitive to the increase of interface properties as shown in Figure 21(b). Conversely, when the interface parameters are decreased by 50 and 80%, the total kinetic energy is increased while energy dissipated by delamination is decreased. Even though the latter energies appear to be sensitive to the reduction in interface parameters, the final residual velocity remain almost unchanged. This can be explained by the fact that a decrease of energy due to delamination is associated with an increase of the kinetic energy, which results in a very slight change in the residual velocity at the end of the impact process. Concurrently, it should be noticed that the dissipation due to interply delamination damage remains still low compared to the other energy dissipation modes.

From the above, we can infer that the present sensitivity analysis has found the global internal energy trend to be insensible to the interface parameters since the contribution of these parameters does not affect the global energy balance and projectile velocity trends.

Considering the damage patterns associated with the interface parameters used in cases 1, 2 and 4, the projected areas of interply delamination damage are plotted for the interfaces 5, 7, 13 and 16 in Figure 22. From these contours, it is seen that the predicted damage evolution parameter

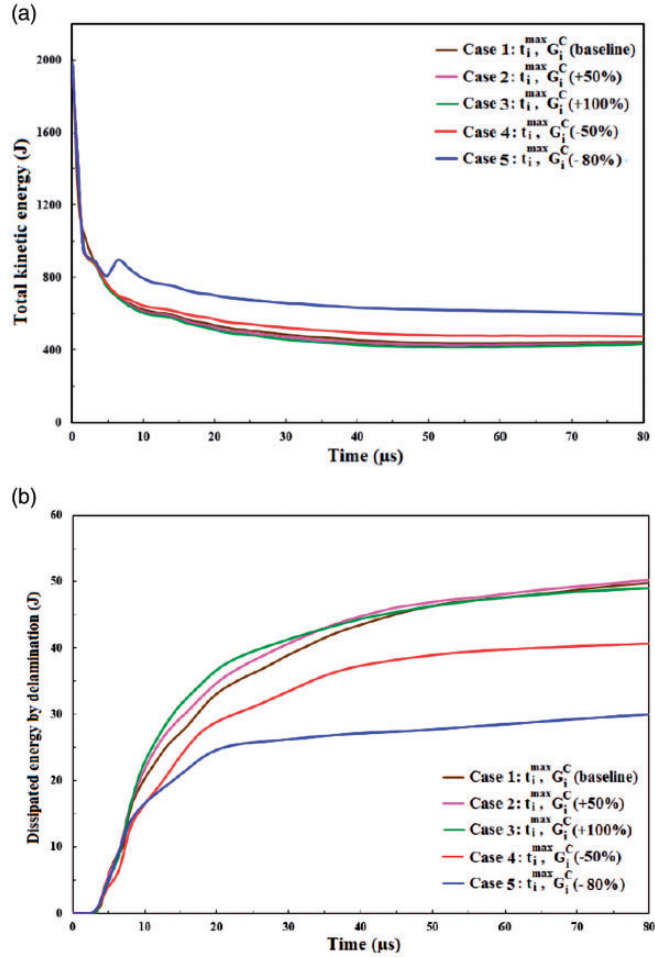


Figure 21. Influence of interlaminar strength and fracture toughness parameters on (a) kinetic energy and (b) energy dissipation due to delamination, at 1980J impact energy.

CSDMG is positively correlated to the delamination interface properties. At low values of t_i^{\max} and G_i^C (case 4, Figure 22(c)), the largest delamination damaged areas are pronounced. Comparatively, at high values of interface parameters (case 2, Figure 22(b)), delamination areas are confined to a small zone localized around the perforated hole border. The difference in the delamination damage spread is certainly attributed to the resistance offered by laminate due to the increase in interlaminar interface strength and its fracture properties.

In fact, the interface property that determines the initial stiffness of the interface K_i is obtained under the assumption that the interface is a quasi-rigid connection within the elastic regime with high initial penalty values of $K_i=10^6$ MPa/mm for loading mode I, II, III (see Table 3). It is therefore necessary to examine the effect of decreasing this parameter on the overall target response in terms of the totally absorbed energy or rather the obtained residual velocity. As displayed in Figure 23, the reduction in the initial stiffness from $K_i=10^6$ MPa/mm to $K_i=10^4$ MPa/mm results in rising the projectile residual velocity by about 5%. In the meantime, while continuing decreasing the

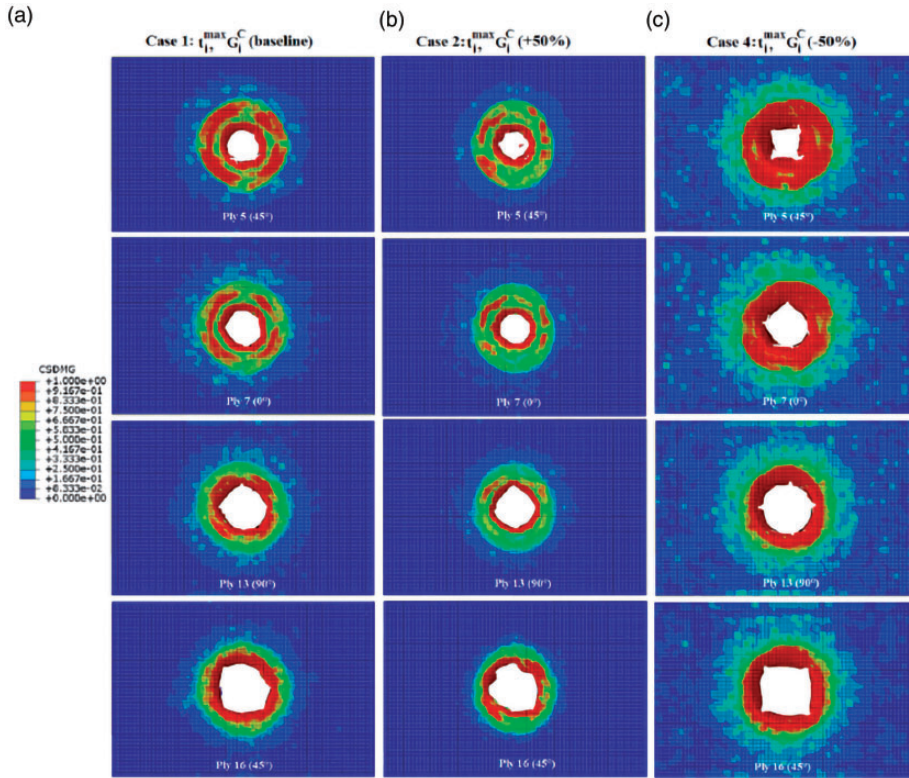


Figure 22. Influence of delamination interface properties (t_i^{\max} and G_i^C) on degree of delamination growth at 1980J impact energy. Red areas indicate full interply delamination.

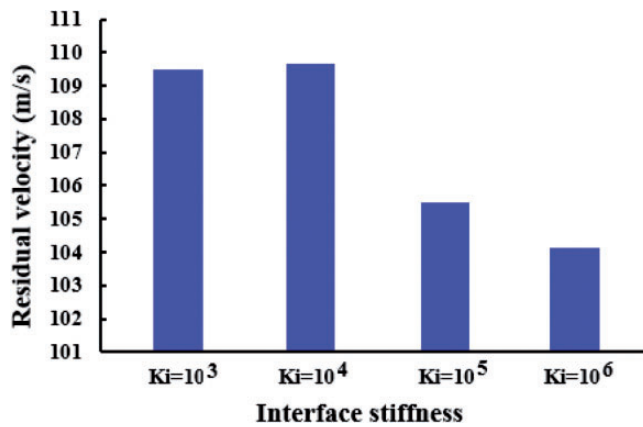


Figure 23. Influence of interface stiffness K_i on the projectile residual velocity at 1980J impact energy.

interface cohesive stiffness below 10^4 MPa/mm, the residual velocity of the projectile remains almost stable. Consequently, we can deduce that the enhancement of the interface penalty stiffness within certain limits could improve the resistance to penetration, and thus lead to lower residual velocities. This can be attributed to the retard of delamination damage initiation and thus certainly retarding the degradation of interface stiffness because of increasing the interface stiffness. As long as the delamination initiation is related to interface stiffness (equations (28) and (29)), before damage initiation, the interface is intact and when has a large initial penalty stiffness, the delamination initiation is delayed and ultimately leads to more dissipated energy.

Summary and conclusions

In this contribution, by means of advanced methods within the framework of the finite element method, an effective modeling approach was presented to simulate the ballistic perforation behaviors of ceramic/composite panels impacted by a non-deformable projectile. This study has mainly covered the impact behavior of alumina/glass WFRP composite target in a two-phase research. The first phase has examined the ballistic impact behavior and ballistic performance of the target system in terms of energy absorption capability. The second phase has involved the investigation of component-level impact characteristics and failure mechanisms of the alumina frontal face and glass composite back-support. The extent and pattern of impact damage with respect to projectile velocity were determined for the target components and the target itself. The study showed that shell continuum element based modeling strategy for composite laminate in combination with a solid element approach for ceramic permits the computational effort to be kept within reasonable bounds.

Based on the constitutive material models development procedure used and the results of the subsequent computational analyses, the following main summary remarks and conclusions can be drawn:

1. The roles of alumina hard-face and a glass composite backing in providing the necessary ballistic resistance of the ceramic/composite hybrid target has been revealed through the use of a non-linear dynamic computational analysis of the target penetration problem.
2. Simulations performed with various impact energies revealed that the ceramic model (Johnson–Holmquist) adopted does present all the failure mechanisms involved and the composite model adopted can successfully predict the intraply damage due to fiber tension and fiber compression along the principal fiber directions, and matrix damage due to shear loading. Concurrently, among the adjacent surfaces, the interlaminar damage based on cohesive zone model was successfully predicted.
3. The temporal evolutions of the pressure contours and material deformation/damage status in the alumina/composite target were thoroughly investigated under different ballistic impact energies. In the early phase of the impact, the response of the target was governed by the alumina hard-face. When the target was impacted, a compressive wave travels from the front to the back face and upon reaching the interface between alumina and composite, a negative pressure zone develops at the rear side of the alumina. Then the wave reflects and becomes a tensile wave which breaks the alumina in tension. A zone subjected to negative pressure was also observed within the composite plies. In the later stages, considerably larger regions of alumina and composite were subjected to both the negative pressure and positive pressure, which structurally fail either through pulverizing due to compression and/or tensile failure due to the negative pressure.

4. Within the alumina hard face layer, it was demonstrated that at early stage of impact, the density of cracks was much higher beneath the impact zone in both front and back sides, thus, a higher number of incipient fragments were developed. After that, as time progresses, the damage is spread out to a larger area on front side compared to the rear side. The failure status in the alumina layer was dominated by the damage caused by the radial, cone and transverse cracking, shear plugging and pulverization of alumina.
5. Within the glass WFRP backing laminate, it has been revealed that, for a high velocity ballistic impact, delamination occurs during the damage initiation and appears at several interfaces nearby the impacted side of the target. After that, fiber breakage and matrix cracking appear, while delamination continuously extends in thickness direction until the laminate completely fails. As a result, on the backside of the target, the failure emerged to be dominated by the spalling and petalling of composite backing laminate with plug formation.
6. From qualitative characterization of fracture mechanisms developed in the composite laminate, it has been disclosed that the final stage of ballistic impact is dominated by fiber tensile damage and fiber compressive damage followed by matrix shear damage.
7. The surface based cohesive behavior used to model the interface debonding between alumina-composite and delamination between individual plies of composite laminate was demonstrated at different impact energies. It turned out that the interlaminar damage variable and the dissipated energy by delamination were almost zero during the first few microseconds. Thenceforth, the energy dissipation caused by interlaminar damage of the interfaces has increased as the impact energy grows.
8. Owing to the complexity of interface delamination mechanism, qualitative assessment of the adhesion was crucial for characterizing the delamination growth and the critical delamination size under ballistic impact. The projected interlaminar damage areas disclosed that the interface damage mainly occurs at the areas around the impact point and the delamination damage contour shape is mostly circular for all interfaces and delamination damage evolution degree are increasing in size along the direction of the impact as time progresses. Besides, in viewing the overall delaminated areas, it was remarked that the delamination damage pattern was more conical in shape.
9. The components of the total energy dissipation were discussed in more thorough details, beginning with the total internal energy (E_{IE}) and its dissipation into E_{PD} , E_{SE} , E_{AE} and E_{DMD} , proceeding to the energy dissipated through ceramic/composite panels' vibration and its relation to the projectile residual kinetic energy, and ending with the contribution of each individual energy absorbing mechanisms concerning the alumina frontal layer and composite back panels.
10. From the conducted energetic analysis under different ballistic impact energies, it has emerged that most of the energy due to impact is absorbed in the form of inelastic deformation, followed respectively by the energy absorbed due to panels' vibration, the elastic strain energy stored within the target, the viscous dissipation, the artificial strain energy and a few less other energies dissipated in the form of delamination, frictional and contact penalty.
11. From the parametric study on friction, it has been found that the friction coefficients did not modify the global response of the ceramic/composite target and layer-to-layer friction (interfacial friction) did not have an important effect on the projectile residual speed, however a slight increment in target-to-projectile friction coefficient resulted in some benefits in terms of ballistic performance (reduction of residual velocity).
12. From the sensitivity analysis on interface properties, it became apparent that the global internal energy trend is insensible to the interface strength (t_i^{\max}) and fracture toughness (G_i^C) since the contribution of these parameters does not affect the global energy balance and projectile

velocity trends. However, it was observed that the reduction in the initial stiffness (K_i) resulted in rising the projectile residual velocity.

13. Eventually, for the preliminary and early stage of design process, the current methods provide an efficient approach for numerical predictions of ballistic impact responses of hybrid ceramic/composite targets and help in reducing the experimental effort associated with their design.

Declaration of conflicting interests

The author(s) declared no potential conflicts of interest with respect to the research, authorship, and/or publication of this article.

Funding

The author(s) disclosed receipt of the following financial support for the research, authorship, and/or publication of this article: This work was performed in the framework of the French DGA (Direction Générale de l'Armement) military funding project called "ENSEMBLE".

ORCID iD

Ibrahim Goda  <https://orcid.org/0000-0001-5508-0261>

References

- Abaqus® (2014) 6.12 Analysis User's Manual. Dassault Systèmes.
- Andrew JJ, Srinivasan SM, Arockiarajan A, et al. (2019) Parameters influencing the impact response of fiber-reinforced polymer matrix composite materials: A critical review. *Composite Structures* 224: 111007.
- Bai Y and Jin W-L (2016) Marine composite materials and structure. In: *Marine Structural Design*. 2nd ed, pp.19–37. Oxford: Butterworth-Heinemann Elsevier. Available at: <https://doi.org/10.1016/C2013-0-13664-1>
- Bandaru AK and Ahmad S (2013) Numerical simulation of progressive damage of laminated composites under ballistic impact. In: Deodatis, Ellingwood & Frangopol (Eds) *Safety, Reliability, Risk and Life-Cycle Performance of Structures and Infrastructures*. Milton Park, UK: Taylor & Francis Group. ISBN 978-1-138-00086-5.
- Bandaru AK, Vetiyatil L and Ahmad S (2015) The effect of hybridization on the ballistic impact behavior of hybrid composite armors. *Composites Part B: Engineering* 76: 300–319.
- Benloulou ISC and Sanchez-Galvez V (1998) A new analytical model to simulate impact onto ceramic/composite armors. *International Journal of Impact Engineering* 21(6): 461–471.
- Bondyra A, Klasztorny M and Muc A (2015) Design of composite tank covers. *Composite Structures* 134: 72–81.
- Chen Y, Fu K, Hou S, et al. (2018) Multi-objective optimization for designing a composite sandwich structure-under normal and 45° impact loadings. *Composites Part B: Engineering* 142: 159–170.
- Fawaz Z, Zheng W and Behdinin K (2004) Numerical simulation of normal and oblique ballistic impact on ceramic composite armor. *Composite Structures* 63(3–4): 387–395.
- Feli S, Yas MH and Asgari MR (2011) An analytical model for perforation of ceramic/multi-layer planer woven fabric target by blunt projectiles. *Composite Structures* 93(2): 548–556.
- Garcia-Avila M, Portanova M and Rabiei A (2015) Ballistic performance of composite metal foams. *Composite Structures* 125: 202–211.
- Goda I, L'Hostis G and Guerlain P (2019) In-situ non-contact 3D optical deformation measurement of large capacity composite tank based on close-range photogrammetry. *Optics and Lasers in Engineering* 119: 37–55.
- Heimbs S, Heller S, Middendorf P, et al. (2009) Low velocity impact on CFRP plates with compressive preload: Test and modelling. *International Journal of Impact Engineering* 36(10–11): 1182–1193.
- Hetherington JG and Rajagopalan BP (1991) An investigation into the energy absorbed during ballistic perforation of composite armors. *International Journal of Impact Engineering* 11(1): 33–40.

- Higuchi R, Okabe T, Yoshimura A, et al. (2017) Progressive failure under high-velocity impact on composite laminates: Experiment and phenomenological mesomodeling. *Engineering Fracture Mechanics* 178: 346–361.
- Hongkarnjanakul N, Bouvet C and Rivallant S (2013) Validation of low velocity impact modelling on different stacking sequences of CFRP laminates and influence of fibre failure. *Composite Structures* 106(12): 549–559.
- Jena PK, Mishra B, Kumar KS, et al. (2010) An experimental study on the ballistic impact behavior of some metallic armour materials against 7.62 mm deformable projectile. *Materials & Design* 31(7): 3308–3316.
- Johnson AF (2001) Modelling fabric reinforced composites under impact loads. *Composites Part A* 32: 1–2.
- Johnson AF and Simon J (1999) Modeling fabric reinforced composites under impact loads. In *EUROMECH 400: Impact and damage tolerance of composite materials and structures*, Imperial College of Science Technology & Medicine, London, UK.
- Johnson GR and Holmquist TJ (1994) An improved computational constitutive model for brittle materials. *High-Pressure Sci Technol* 1993(Pts 1 and 2): 981–984.
- Krell A and Strassburger E (2008) Hierarchy of key influences on the ballistic strength of opaque and transparent armor. *Ceramic Engineering and Science Proceedings* 28: 45–55.
- Krishnan K, Sockalingam S, Bansal S, et al. (2010) Numerical simulation of ceramic composite armor subjected to ballistic impact. *Composites Part B: Engineering* 41(8): 583–593.
- Kulkarni SG, Gao XL, Horner SE, et al. (2013) Ballistic helmets – Their design, materials, and performance against traumatic brain injury. *Composite Structures* 101: 313–331.
- Kursun A and Senel M (2013) Investigation of the effect of low-velocity impact on composite plates with preloading. *Experimental Techniques* 37(6): 41–48.
- Li X, Ma D, Liu H, et al. (2019) Assessment of failure criteria and damage evolution methods for composite laminates under low-velocity impact. *Composite Structures* 207: 727–739.
- Liao BB and Jia LY (2018) Finite element analysis of dynamic responses of composite pressure vessels under low velocity impact by using a three-dimensional laminated media model. *Thin-Walled Structures* 129: 488–501.
- Liu W, Chen Z, Chen Z, et al. (2015) Influence of different back laminate layers on ballistic performance of ceramic composite armor. *Materials & Design* 87: 421–427.
- Liu W, Chen Z, Cheng X, et al. (2016) Design and ballistic penetration of the ceramic composite armor. *Composites Part B: Engineering* 84: 33–40.
- Lopes C, Seresta O, Coquet Y, et al. (2009) Low-velocity impact damage on dispersed stacking sequence laminates. Part I: Experiments. *Composites Science and Technology* 69(7–8): 926–936.
- López-Puente J, Zaera R and Navarro C (2007) An analytical model for high velocity impacts on thin CFRPs woven laminated plates. *International Journal of Solids and Structures* 44(9): 2837–2851.
- Maimí P, Camanho PP, Mayugo J-A, et al. (2006) A thermodynamically consistent damage model for advanced composites. Technical Report NASA/TM-2006-214282, NASA.
- Mikkor KM, Thomson RS, Herszberg I, et al. (2006) Finite element modelling of impact on preloaded composite panels. *Composite Structures* 75(1–4): 501–513.
- Mitrevski T, Marshall IH, Thomson RS, et al. (2006) Low-velocity impacts on preloaded GFRP specimens with various impactor shapes. *Composite Structures* 76(3): 209–217.
- Mousavi MV and Khoramishad H (2019) The effect of hybridization on high-velocity impact response of carbon fiber-reinforced polymer composites using finite element modeling, Taguchi method and artificial neural network. *Aerospace Science and Technology* 94: 105393.
- Naik NK and Doshi AV (2005) Ballistic impact behavior of thick composites: Analytical formulation. *AIAA Journal* 43(7): 1525–1536.
- Naik NK and Shrirao P (2004) Composite structures under ballistic impact. *Composite Structures* 66(1–4): 579–590.
- Naik NK, Kumar S, Ratnaveer D, et al. (2013) An energy-based model for ballistic impact analysis of ceramic-composite armors. *International Journal of Damage Mechanics* 22(2): 145–187.
- Pandya KS, Pothnis JR, Ravikumar G, et al. (2013) Ballistic impact behavior of hybrid composites. *Materials & Design* 44: 128–135.

- Park SJ and Seo MK (2012) Carbon fiber-reinforced polymer composites: preparation, properties, and applications. In: Thomas S, Kuruville J, Malhotra SK, et al. (Eds.) *Polymer Composites: Volume 1, Wiley-VCH Verlag GmbH & Co. KGaA* 135. Available at: <http://dx.doi.org/10.1002/9783527645213.ch5>
- Pernas-Sánchez J, Artero-Guerrero J, Viñuela JZ, et al. (2014) Numerical analysis of high velocity impacts on unidirectional laminates. *Composite Structures* 107: 629–634.
- Phadnis VA, Pandya KS, Naik NK, et al. (2013) Ballistic impact behaviour of woven fabric composite: Finite element analysis and experiments. *Journal of Physics: Conference Series* 451: 012019.
- Rahbek DB and Johnsen BB (2019) Fragmentation of an armour piercing projectile after impact on composite covered alumina tiles. *International Journal of Impact Engineering* 133: 103332.
- Rashed A, Yazdani M, Babaluo AA, et al. (2015) Investigation on high-velocity impact performance of multi-layered alumina ceramic armors with polymeric interlayers. *Journal of Composite Materials*. Epub ahead of print 20 December 201550(25): 3561–3576. <https://doi.org/10.1177/0021998315622982>
- Safri SNA, Sultan MTH, Jawaid M, et al. (2018) Impact behaviour of hybrid composites for structural applications: A review. *Composites Part B: Engineering* 133: 112–121.
- Sastry YBS, Budarapu PR, Krishna Y, et al. (2014) Studies on ballistic impact of the composite panels. *Theoretical and Applied Fracture Mechanics* 72: 2–12.
- Schoeppner G and Abrate S (2000) Delamination threshold loads for low velocity impact on composite laminates. *Composites Part A: Applied Science and Manufacturing* 31(9): 903–915.
- Schwab M and Pettermann HE (2016) Modelling and simulation of damage and failure in large composite components subjected to impact loads. *Composite Structures* 158: 208–216.
- Schwab M, Todt M, Wolfahrt M, et al. (2016) Failure mechanism based modelling of impact on fabric reinforced composite laminates based on shell elements. *Composites Science and Technology* 128: 131–137.
- Schwab M, Todt M, Tauchner J, et al. (2018) Modeling, simulation, and experiments of high velocity impact on laminated composites. *Composite Structures* 205: 42–48.
- Serjoui A, Chi R, Zhang Z, et al. (2015) Experimental validation of BLV model on bi-layer ceramic-metal armor. *International Journal of Impact Engineering* 77: 30–41.
- Shanazari H, Liaghat GH, Feli S, et al. (2017) Analytical and experimental study of high-velocity impact on ceramic/nanocomposite targets. *Journal of Composite Materials* 51(27): 3743–3756.
- Shokrieh MM and Javadpour GH (2008) Penetration analysis of a projectile in ceramic composite armor. *Composite Structures* 82(2): 269–276.
- Signetti S and Pugno NM (2014) Evidence of optimal interfaces in bio-inspired ceramic-composite panels for superior ballistic protection. *Journal of the European Ceramic Society* 34(11): 2823–2831.
- Silva MAG, Cismaşiu C and Chiorean CG (2005) Numerical simulation of ballistic impact on composite laminates. *International Journal of Impact Engineering* 31(3): 289–306.
- Talib AA, Abbud L, Ali A, et al. (2012) Ballistic impact performance of kevlar-29 and Al₂O₃ powder/epoxy targets under high velocity impact. *Materials & Design* 35: 12–19.
- Tan W, Falzon BG, Chiu LN, et al. (2015) Predicting low velocity impact damage and compression-after-impact (CAI) behaviour of composite laminates. *Composites Part A: Applied Science and Manufacturing* 71: 212–226.
- Tasdemirci A, Tunusoglu G and Güden M (2012) The effect of the interlayer on the ballistic performance of ceramic/composite armors: Experimental and numerical study. *International Journal of Impact Engineering* 44: 1–9.
- Tham CY, Tan VBC and Lee HP (2008) Ballistic impact of a KEVLAR[®] helmet: Experiment and simulations. *International Journal of Impact Engineering* 35(5): 304–318.
- Tita V, Carvalho J and Vandepitte D (2008) Failure analysis of low velocity impact on thin composite laminates: Experimental and numerical approaches. *Composite Structures* 83(4): 413–428.
- Walsh SM, Scott BR and Spagnuolo DM (2005) The development of a hybrid thermoplastic ballistic material with applications to helmets. U.S. Army research laboratory, *Aberdeen Proving Ground, MD. ARL-TR-3700*, p.19.
- Wang FS, Ji YY, Yu XS, et al. (2016) Ablation damage assessment of aircraft carbon fiber/epoxy composite and its protection structures suffered from lightning strike. *Composite Structures* 145: 226–241.

- Yamada M, Tanabe Y, Yoshimura A, et al. (2011) Three-dimensional measurement of CFRP deformation during high-speed impact loading. *Nuclear Instruments and Methods Physics Research Section A: Accelerators, Spectrometers, Detectors and Associated Equipment* 646(1): 219–226.
- Yossifon G, Yarin AL and Rubin MB (2002) Penetration of a rigid projectile into a multi-layered target: Theory and numerical computations. *International Journal of Engineering Science* 40(12): 1381–1401.
- Yen CF (2012) A ballistic material model for continuous-fiber reinforced composites. *International Journal of Impact Engineering* 46: 11–22.
- Zaera R (2011) Ballistic impacts on polymer matrix composites, composite armor, personal armor. In: Abrate S (ed) *Impact Engineering of Composite Structures*. 526th ed. Vienna: Springer, pp.305–403.
- Zhang XF and Li YC (2010) On the comparison of the ballistic performance of 10% zirconia toughened alumina and 95% alumina ceramic target. *Materials & Design* 31(4): 1945–1952.
- Zinszner JL, Forquin P and Rossiquet G (2015) Experimental and numerical analysis of the dynamic fragmentation in a SiC ceramic under impact. *International Journal of Impact Engineering* 76: 9–19.